PLUME-RIDGE INTERACTION ALONG THE GALÁPAGOS SPREADING CENTER, 90°30'W TO 98°W: A HYDROUS MELTING MODEL TO EXPLAIN VARIATIONS IN OBSERVED GLASS COMPOSITIONS

A THESIS SUBMITTED TO THE GRADUATE DIVISION OF THE UNIVERSITY OF HAWAI'I IN PARTIAL FULFILLMENT OF THE REQUIREMENTS FOR THE DEGREE OF

MASTER OF SCIENCE

IN

GEOLOGY AND GEOPHYSICS

AUGUST 2003

By
Buffy Jolene Cushman

Thesis Committee:

John Sinton, Chair
Richard Hey
Garrett Ito
John Mahoney
Sarah Sherman

Abstract

The Galápagos Spreading Center (GSC) between 90°30'W and 98°W shows manifestations of its interaction with the nearby Galápagos plume by way of variations in lava geochemistry, crustal thickness, and morphology along the ridge axis. Rock samples with an average spacing of ~9 km were analyzed for major elements and dissolved H_2O. Samples were classified as E-MORBs, T-MORBs, or N-MORBs based on K/Ti ratios. E-MORBs dominate the GSC east of 92.6°W. T-MORBs are mainly found between 92.6°W and 95.5°W. West of the propagating rift tip at 95.5°W, N-MORBs dominate. High K/Ti E-MORBs are also characterized by higher H_2O, Al_2O_3, and Na_2O, and lower FeO*, SiO_2, and CaO/Al_2O_3 relative to N-MORB at similar values of MgO. These compositional characteristics are consistent with lower mean extents of partial melting relative to N-MORB. We developed a melting equation to assess the change in lava composition and mean fraction of partial melting ($\overline{F}$) produced by contributions from the zone of hydrous melting whose presence is caused by the depression of the mantle solidus by H_2O. We use our hydrous melting equation to model the source composition, the depth of the additional hydrous melting zone, the productivity in the hydrous region, and the upwelling rate that may combine to match our measured crustal thickness values and concentrations of K, Na_2O, H_2O, and Ti in lavas from the GSC. Model results indicate that GSC N-MORBs were created by $\overline{F}$ ~0.06 from a source with ~34±1 ppm K, 133±3 ppm H_2O, 2250±50 ppm Na_2O, and 1050±25 ppm Ti. E-MORB values can be predicted in a number of ways. Higher upwelling rates in the E-MORB region require less source enrichment than low upwelling rates. Upwelling rate has the strongest effect on $\overline{F}$. The crustal thickness and glass compositional variations in the "enriched" region of the GSC can best be explained by only a slight increase in the temperature of the mantle (11±11°C), coupled with a

moderately enriched mantle source and upwelling of 1.5-3.5 times passive upwelling rates. The transitional region requires only slight upwelling (U_w/U_0 =1.5) and a source enriched only in K.

Table of Contents

List of Tables

List of Figures

1. Introduction

The global mid-ocean ridge system is affected by near- and on-axis hotspots, commonly thought to represent mantle plumes. Mantle plumes can impose large physical and chemical anomalies on otherwise normal ridges; the manifestations of such anomalies provide insight into ridge and mantle processes. Processes that often cannot be studied as well from a "normal" mid-ocean ridge include mantle flow and melting, source mixing, and the effects of variable magma supply on axial morphology, basalt chemistry, and crustal accretion. The Galápagos Spreading Center (GSC), with its intermediate spreading rate and off-axis plume, provides an excellent setting for studying plume-ridge interaction.

The nearly east-west trending GSC separates the Cocos and Nazca plates in the eastern equatorial Pacific (Figure 1). The full opening rate of the GSC increases from 44 mm/yr at 98°W to about 67 mm/yr at 83°W [*DeMets et al.*, 1994], where it terminates against the Panama Fracture Zone. Spreading rate at 91°W is ~56 mm/yr [*DeMets et al.*, 1994]. At 91°W the GSC lies ~200 km north of the Galápagos Archipelago, the western end of which marks the probable center of the Galápagos mantle plume [*Geist*, 1992; *White et al.*, 1993]. Effects of the nearby hotspot are manifest in the regional bathymetric swell that extends ~1300 km along the ridge and peaks near 91°W, where the axial depth is more than 1 km shallower than portions of the ridge far from the hotspot, and in a regional mantle-Bouguer gravity anomaly that reaches its minimum (-70 mGal) near 91°W [*Canales et al.*, 2002]. The hotspot effect can also be seen in variations in axial morphology along the ridge, because intermediate-spreading ridges are most susceptible to small changes in magma supply [*Sinton and Detrick*, 1992; *Phipps Morgan and Chen*,

1993]. Within ~350 km of the Galápagos hotspot the GSC has an axial high morphology; with increased distance from the hotspot it changes to a transitional morphology, ultimately becoming a Mid-Atlantic-Ridge-like rift-valley farthest from the hotspot [*Canales et al.*, 1997] (Figure 2).

Several authors have examined the large-scale geochemical variations along the GSC, from 83°W to 101°W (see *Schilling et al.*, 1982; *Fisk et al.*, 1982; *Verma and Schilling*, 1982; *Verma et al.*, 1983). These authors showed that rocks with high $^{87}Sr/^{86}Sr$ and incompatible element concentrations and low $^{143}Nd/^{144}Nd$ are confined to the region of the ridge closest to the hotspot, bounded on both sides by propagating ridges. Normal mid-ocean ridge basalts (MORBs) (i.e., those most similar to MORBs found in portions of the ocean-ridge system that are not associated with any nearby hotspots) are found west and east of the 95.5°W and 85°W propagating rifts, respectively. These authors argued for a variably enriched mantle source nearest the hotspot, between 95.5°W and 85°W.

The Galápagos Plume Ridge Interaction Multidisciplinary Experiment (G-PRIME, or G') was a comprehensive, multidisciplinary study of the GSC that examined both medium-scale and large-scale variations along an ~800 km-long portion of the ridge between 90.5°W, approximately due north of islands Fernandina and Isabela, and 98°W, the region of the GSC that is considered to be "normal" MORB. G' data collection took place in April and May 2000, on the R/V Maurice Ewing leg EW0004. Data collected include detailed bathymetry, seismic refraction, reflection, and magnetics data, as well as an extensive rock collection for major element, trace element, isotopic, and petrographic analysis.

Three wide-angle seismic refraction experiments conducted as part of G' provide estimates of crustal thickness from three different portions of the GSC [*Canales et al.*, 2002]. Seismic reflection data gathered across- and along-axis in the region east of 95°W further constrain crustal thickness, as well as the depth of layer 2A and axial magma chambers, where present. *Detrick et al.* [2002] and *Blacic et al.* [in prep] report these results.

Ninety-one dredge and wax core stations were successfully sampled. One sample was collected from the transform fault at 90.5°W; all other sampling stations were at the ridge axis, with an average of ~9 km between stations (Figure 2, Table 1). Sampling locations were chosen based on multibeam bathymetric data collected during the cruise. In this paper we report major and minor element and H_2O data for G' glasses. In addition, we reanalyzed selected glasses from the 95.5°W area [*Christie and Sinton*, 1981, 1986; *Yonover*, 1989; *Hey et al.*, 1992] in order to ensure uniform data quality and to augment the G' data set.

2. Sample Treatment and Analyses

Glass compositions were measured using the University of Hawaii Cameca SX-50, five-spectrometer electron microprobe. Major and minor element analyses were obtained on glass chips from ~200 individual samples. Alvin samples and Atlantis dredge samples [*Hey et al.*, 1992] were re-analyzed using the same procedures. Reported analyses are averages of ten spots collected from three to six glass chips per sample, using an accelerating voltage of 15 kV, 10 nA beam current, and 10 μm beam diameter. Peak counting times were 110 seconds for P; 50 seconds for Mn; 40 seconds for Fe; 30

seconds for Mg, Al, Ca, and Ti; and 20 seconds for Na. Background counting times were 90 seconds for P; 30 seconds for K; 20 seconds for Mn; 10 seconds for Na, Ca, and Fe; and 5 seconds for Mg, Al, Si, and Ti. Samples were calibrated using Makaopuhi glass standard A-99 (Mg, Si, Ti, Fe), Juan de Fuca glass standard VG-2 (Na, Al, Ca), and mineral standards apatite (P) and orthoclase (K). A PAP-ZAF matrix correction was applied to all analyses.

The number of individual samples analyzed per dredge varied between 1 and 12, depending on the size of the dredge haul. Dredges were dragged over ~200-500 meters of seafloor, so it is possible that rocks in a dredge haul include samples from more than one lava flow. Individual samples from each station with compositions that agreed within ~5-10% in the low-abundance oxides K_2O, P_2O_5, TiO_2, and Na_2O were designated as a single group. High-abundance element concentrations were compared for consistency of the groupings; in all cases some variance between groups is observed in all elements. Most dredges contain only one group; the maximum number of groups in a dredge is three (dredges 41, 55). Once groups were determined, all analyses for samples from that group were averaged (Table 2). Each group probably represents a single lava flow or group of closely related flows. Uncertainty was estimated from standard deviations among all samples within a group, and then averaged for all of the groups represented by more than one sample. These uncertainties are also listed in Table 2.

Based on major element composition and along-axis locations, one glass sample from each of 42 of the groups was analyzed for H_2O. Concentrations of dissolved water were measured using infrared spectroscopy, following the procedures of *Dixon and Clague* [2001]. Glass chips were doubly polished to a thickness between 20 and 200

microns. Infrared transmission spectra in the 4000-1200 cm^{-1} (2.5 to 8.3 mm) range were collected at the University of Miami using an infrared microscope attachment to a Brüker IFS-66 FTIR spectrometer, a Globar source, a KBr beam splitter, a HgCdTe detector, and a mirror velocity of 1.57 cm/s. Spot sizes ranged from 70-200 microns. Typically, 2024 scans were collected for each spectrum. The spectrum of a tholeiitic glass was subtracted from the sample spectrum as a background correction. Absorbance measurements for the molecular water bands were made on reference-subtracted spectra using interactive baseline and curve-fitting routines available in the OPUS software on the Brüker IFS-66 infrared spectrometer. This technique makes use of fundamental peak shape information for the molecular water bands based on well-defined standard bands with flat backgrounds. The molecular water band at 1630 cm^{-1} was modeled assuming a gaussian shape with a full width at half height of ~55 cm^{-1}.

H_2O concentrations were derived from the spectra using Beer-Lambert law calibration (see review in *Ihinger et al.*, 1994). The thickness, or path length, was measured with a digital micrometer with a precision of ± 1-2 mm. Glass density was calculated for each sample using the Gladstone-Dale rule and the Church-Johnson equation as described by *Silver et al.* [1990]. The molar absorptivity for total dissolved water using the fundamental OH stretching band at 3535 cm^{-1} is not strongly compositionally dependent for basaltic compositions; we used a value of 63 ± 3 l/mol-cm (P. Dobson, S. Newman, S. Epstein, and E. Stolper, 1988, unpublished results). Molar absorptivity for the molecular water band at 1630 cm^{-1} is 20 ± 5 l/mole-cm [*Dixon et al.*, 1997].

Precision of the analyses is about ± 2% for total water and ± 7 to 10% for molecular water. The accuracy of the total water analyses is the same as reported by *Dixon et al.* [1991] (about ± 10%). Because of the larger uncertainty in the compositional dependence of the molar absorptivity for water dissolved as molecular water in silicate glasses, the accuracy of the molecular water analyses is estimated to be about ± 20%.

3. Observations

3.1. Classification of MORB-types

Glass compositions vary significantly as a function of MgO content. To assess potential differences in parental magma compositions, we use K/Ti ratios to divide our samples (Figure 3) [*Schilling et al*, 1983; *Hekenian et al.*, 1989; *Sinton et al.*, 1991; *Langmuir et al.*, 1992], because K/Ti is relatively unaffected by fractionation processes at MgO values greater than that at which FeTi oxide appears as a fractionating phase (~4.5 wt% MgO in G' samples, see Figure 4c, e). G' samples can be divided into three general types: enriched (E-) MORB, with K/Ti ratios >0.15 and K_2O contents >0.20 wt %; transitional (T-) MORB, with K/Ti ratios mainly between 0.09 and 0.15; and normal (N-) MORB, with K/Ti ratios < 0.09 (Figure 3). K/Ti ratios alone effectively discriminate the three sample groups. Most MORBs with K/Ti > 0.15 have K_2O abundances > 0.20 wt.%, and are therefore "enriched" in the more incompatible element, K. However, two sample groups (15D and 39D-b) have K/Ti > 0.15 but K_2O < 0.20 wt.%. On most plots, including those involving trace element data not reported here, these samples follow trends associated with T-MORBs. Thus, we restrict the definition of E-MORB in this paper to sample groups with K/Ti > 0.15 and K_2O > 0.20 wt.%.

Although the threefold division accounts for most of the compositional diversity, it is apparent that significant variability at constant MgO, especially in SiO_2 and Al_2O_3, is present within the E- and T-MORB types (Figure 4e-i). We have therefore subdivided these types as follows: "regular" E-MORBs (hereafter E1-MORBs) fall on a trend sub-parallel to the N-MORB and T-MORB trends. E2-MORBs have anomalously low SiO_2 and high CaO/Al_2O_3, the latter because of both lower CaO and higher Al_2O_3 than E1-MORBs. T2-MORBs have slightly higher incompatible element values, particularly K_2O, relative to "regular" T1-MORBs. T3-MORBs have low CaO/Al_2O_3 ratios, and low SiO_2, as well as higher Na_2O and K_2O than T1-MORBs.

3.2. Compositional Variations

The least differentiated of all G' samples are N-MORBs, which have MgO values that range from 6.9 wt. % MgO to almost 10 wt.% MgO. The N-MORBs are characterized by low concentrations of elements that are incompatible during mantle melting: $\leq$ 0.08 wt.% K_2O, 1.67-2.56 wt.% Na_2O, 0.77-1.68 wt.% TiO_2, 0.05-0.12 wt.% P_2O_5. Slight changes in the slopes of MgO versus CaO, SiO_2, and CaO/Al_2O_3 for N-MORBs show that plagioclase joins olivine in the fractionating assemblage between ~8.0 and 8.5 wt.% MgO. N-MORBs have the lowest H_2O concentrations of all G' samples, with no values greater than 0.22 wt.% H_2O (Figure 5a). These "normal" MORB values are typical of, or even slightly lower than, H_2O values found along other "normal" portions of the global mid-ocean ridge system [*Michael*, 1988, 1995; *Dixon et al.*, 1988; *Danyushevsky et al.*, 2000].

The T-MORBs are slightly more differentiated than the N-MORBs as a group, with MgO contents ranging from 6.1 to 9.3 wt.%, and with the bulk of the samples having MgO < 8.0 wt.% (Figure 4). The T-MORBs are most distinct from the N-MORBs in K_2O, giving rise to their higher K/Ti ratios. The T-MORBs have average values of incompatible species Na_2O, P_2O_5, TiO_2, and FeO* (Fe_2O_3 wt.% and FeO wt.% all reported as FeO wt.%) higher than in the N-MORBs because they tend to be less fractionated, but the differentiation trends are collinear. Differentiation trends for the T-MORBs are also collinear with those for the N-MORBS for CaO, FeO*, Al_2O_3, and SiO_2. As with the N-MORBs, changes in the slope of CaO and SiO_2 trends for the T-MORBs indicate plagioclase crystallization beginning between ~8.0 and 8.5 % MgO.

T2-MORBs differ from T1-MORBs in CaO/Al_2O_3, mostly because of lower CaO. T2-MORBs are also slightly enriched in TiO_2, K_2O, and H_2O relative to T1-MORBs. T3-MORBs have much lower CaO/Al_2O_3 than T1-MORBs, as a result of both lower CaO and higher Al_2O_3 at a given MgO value. T3-MORBs have significantly lower SiO_2 than T1-MORBs, and are slightly enriched relative to T1-MORBs in Na_2O, K_2O, TiO_2, P_2O_5, and H_2O.

The E-MORBs as a group are more differentiated than the N- and T-MORBs, with MgO contents ranging to values as low as 3.3 wt.% (Figure 4). E-MORBs are enriched relative to N- and T-MORBs in the elements K_2O, Na_2O, P_2O_5, and H_2O. TiO_2 values are slightly higher at a given MgO value in E-MORBs than T-MORBs. Lower relative FeO* and SiO_2, and higher Al_2O_3 values also characterize E-MORBs. E1-MORB Al_2O_3 and CaO/Al_2O_3 variations indicated that clinopyroxene joins the fractionating

assemblage near ~5.5-6.0 wt.% MgO. FeO and TiO_2 plots show that oxides fractionated from E-MORB magmas with less than ~ 4.5 wt.% MgO.

E2-MORBs show the same relationships to E1-MORBs as do T3-MORBs relative to T1-MORBs: they have lower CaO/Al_2O_3, as a result of both lower CaO and higher Al_2O_3 at a given MgO value, and significantly lower SiO_2. E2-MORBs are among the least differentiated rocks of the E-MORBs. E2-MORBs also tend to have slightly higher concentrations of incompatible elements Na_2O, K_2O, TiO_2, and P_2O_5 than E1-MORBs at the same MgO value.

Samples from group 78D are scoria—all glass with >60% vesicularity. Group 78D, with 6.15 wt.% MgO, is classified as an E2-MORB based on its low SiO_2 content and high values of Na_2O, K_2O, TiO_2, and P_2O_5 relative to E1-MORBs (Figure 4). This sample group has CaO, and Al_2O_3 compositions that are more similar to E1-MORBs, but H_2O content that is unlike E1- or E2-MORBs. H_2O, at 0.18 wt.%, appears to have degassed, consistent with its high vesicle content.

H_2O contents of GSC samples correlate positively with K_2O contents (Figure 5b), indicating that H_2O behaves incompatibly, with bulk distribution coefficient (D) slightly higher than that of K_2O. This result is consistent with the conclusions of *Michael* [1988, 1995], *Dixon et al.* [1988], and *Danyushevsky et al* [2000], who argue that water in basalts behaves incompatibly during melting and crystallization, with a D of ~0.01. The strong positive correlation between K_2O and H_2O suggests that the same processes that affect abundances of other incompatible elements in MORB also control H_2O. Additionally, this excellent correlation is consistent with negligible contamination of the

magmas by seawater, which should elevate H_2O relative to K_2O in a non-systematic way [*Danyushevsky et al.*, 2000].

3.3. $MgO_{8.0}$ Calculations

In order to determine parental magma compositions for each magma type, we have adjusted our data for the effects of low-pressure differentiation by calculating oxide values of MgO = 8.0 wt.% [*Klein and Langmuir*, 1987]. The adjusted values are indicated hereafter with a subscript of 8.0. This adjustment allows for comparisons among lava types as well as with global MORB data sets. We used least-squares regression to quantify the oxide variations versus MgO for each type and adjusted all data using the slope of the regression. Samples with MgO contents >8.5wt% or <3.5wt% were excluded; thus, the empirical line along which we adjusted the data probably represents cotectic crystallization of olivine and plagioclase ± pyroxene only. Separate slopes were calculated for each of the three general magma types (i.e., N-, T1- and E1-MORBs). Lines were fitted through SiO_2, Al_2O_3, FeO*, and CaO data. For incompatible elements that obey Henry's law, perfect fractional crystallization produces a curve, element enrichment versus fraction of liquid remaining in the magma, that is effectively the form of a power law equation. Accordingly, best-fit power-law curves were used for adjusting K_2O, Na_2O, TiO_2, P_2O_5, and H_2O data.

Regression of the E2-MORB data alone would not produce a statistically valid regression due to the small number of data points. Thus, we adjusted E2-MORBs using the same slope as for the E1-MORBs, assuming that they evolved by similar processes, but from a different parental magma. Similarly, T2- and T3-MORBs were excluded from

the regressions, but oxide values were adjusted using the same slope as used for the T1-MORBs. Details of slope calculations are shown in Table 3.

3.4. Along-Axis Variations

E-MORBs dominate the GSC east of 92.6°W; T-MORBs are mainly found between 92.6°W and 95.5°W (shaded area in Figure 6); only N-MORBs (plus one E2-MORB scoria group) are found west of 95.7°W. The limit of E-MORB occurrence is entirely consistent with the "plume-influenced" "type B" basalts of *Fisk et al* [1982]. *Fisk et al.* [1982] and *Schilling et al.* [1982] also noted petrological differences between basalts from within the "H-zone" (high magnetic amplitude zone [*Anderson et al*, 1975]), which is confined to the region of the GSC between the tips of the propagating rifts at 95.5°W and 85°W, and those outside of it. The boundary separating N-MORB- and T-MORB-dominated provinces in our data coincides with the 95.5°W propagating rift tip (Figure 6a).

The western limit of E-MORB occurrence (excluding sample 78D-scoria), near 92.7°W, coincides with the abrupt transition to an axial high morphology that occurs over an along-axis distance of only about 20 km, rapid shoaling (from west to east) of the axial magma chamber seismic reflector by >1 km, and an approximate halving of the thickness of seismic layer 2A from 0.3-0.5 s two-way travel time (TWTT) (~300-500 m) to 0.15-0.35 s TWTT (~150-350 m) [*Detrick et al.*, 2002]. The westernmost extent of T-MORBs, 95.7°W, corresponds with the propagating rift (PR) system near 95.5°W. The PR tip at 95.5°W marks the boundary between axial rift-valley morphology, to the west, and the region between 95.5°W and 92.7°W, dominated by transitional morphology. With the

exception of anomalous E2-MORB 78D-scoria, only N-MORBs are found west of 95.7°W.

Within the N-MORB region, $FeO^*_{(8.0)}$ and $TiO_{2(8.0)}$ decrease slightly from west to east, while $SiO_{2(8.0)}$ increases. In the 95.5°W propagating rift region, between ~ 95.1°W and 95.5°W, $FeO^*_{(8.0)}$ and $TiO_{2(8.0)}$ are elevated relative to the surrounding regions [*Christie and Sinton*, 1981, 1986]; $H_2O_{(8.0)}$ is also high in this region. Mg# (defined as molar MgO/(MgO + FeO*) is bimodally distributed in the region closest to the propagating rift. The group of samples with low Mg# defines a narrow trend that decreases to the west from ~ 94.2°W to the rift tip. Between ~ 94.2°W and the eastern edge of the overlapping spreading center system at ~ 93.1°W, $FeO^*_{(8.0)}$ and $SiO_{2(8.0)}$ are nearly constant, while Mg# is highly variable compared to its narrow range to the west. East of ~ 93.1°W, T-MORB $FeO^*_{(8.0)}$ and $SiO_{2(8.0)}$ values decrease. These trends continue beyond the first occurrence of E-MORBs at 92.7°W until they reach their minima near 91.7°W.

Along-axis variations in elements adjusted to 8.0 wt.% MgO show that the most extreme values are between ~91.7°W and 92.4°W (Figure 6). $K_2O_{(8.0)}$, $TiO_{2(8.0)}$, $Al_2O_{3(8.0)}$, $Na_2O_{(8.0)}$, $P_2O_{5(8.0)}$, and $H_2O_{(8.0)}$ peak in this region, while $FeO^*_{(8.0)}$, $SiO_{2\,(8.0)}$, $CaO_{(8.0)}$, and $CaO_{(8.0)}/Al_2O_{3(8.0)}$ are at their lowest values. We infer that these geochemical features characterize the most plume-influenced rocks.

The apparent K/Ti peak at 91.4°W (Figure 6f) is misleading. It is represented by highly fractionated samples 11D-a and 11D-b, with MgO contents of 3.33 and 3.98 wt.%, respectively. Fractionation of Fe-Ti oxides (see Figure 4c, e) in these magmas produced

high K/Ti values that reflect reduction in the TiO_2 content of the glasses, not enrichment in K_2O.

The fractionation-adjusted maxima and minima are dominated by E2-MORBs—groups 16D, 17D-a, 17D-b, 20D-a, and 20D-b. Samples from dredge 17, at 91.8°W, have the highest $TiO_{2(8.0)}$, $Al_2O_{3(8.0)}$, $Na_2O_{(8.0)}$, and $P_2O_{5(8.0)}$, and the lowest $FeO^*_{(8.0)}$, $SiO_{2(8.0)}$, and $CaO_{(8.0)}/Al_2O_{3(8.0)}$ contents, thus defining the ridge location of greatest plume influence. Sample 26C, at 92.37°W, falls off the general longitudinal trends for $K_2O_{(8.0)}$, K/Ti and $FeO^*_{(8.0)}$. It is the westernmost sample with a very strong plume influence.

Stations 16, 17, and 20, which together define the region of strongest plume influence, are all located between 91.7°W and 92.0°W, at or near the intersection of the GSC with two linear volcanic chains. Linear chains intersect the GSC in four places between the transform fault at ~90.7°W and ~92.2°W, and appear to extend from the Galápagos platform toward the rise axis (Figure 2). The lineaments are characterized by elevated bathymetry, locally creating islands. Although we did not collect samples or bathymetric data from these volcanic chains during the G' project, *Harpp and Geist* [2002] report that rock samples from Wolf and Darwin islands, located along the Wolf-Darwin lineament, which intersects the GSC at ~ 92.2°W, appear more petrologically MORB-like than plume-like.

The greatest geochemical signature of plume influence also coincides with maxima in crustal thickness (7.9 km) and residual swell anomaly (~300 m), and minima in axial depth (<1700m), magma chamber depth (<1.5 km) and residual gravity anomaly (-25 mGal) [*Detrick et al.*, 2002]. These correlated geochemical and geophysical

characteristics are consistent with increased melt production in this region, and the creation of a hotter, weaker axial lithosphere [*Detrick et al.*, 2002].

4. Modeling Hydrous Melting

Compared to N-MORBs, the E-MORBs—which dominate the region closest to the hotspot—are enriched in oxides that are incompatible during melting of mantle peridotite (e.g., K_2O, Na_2O, TiO_2, Al_2O_3, H_2O). As shown by *Schilling et al.* [1982], the relative enrichment is approximately inversely proportional to the *D* for melting of mantle peridotite; i.e., the most incompatible elements are the most enriched. This relationship suggests that variable melting processes are important in controlling the observed distribution along axis [*Fisk et al.*, 1982; *Schilling et al.*, 1982]. *Verma and Schilling* [1982] and *Verma et al.* [1983] showed that Sr and Nd isotope ratios also vary along axis, with the highest $^{87}Sr/^{86}Sr$ and lowest $^{143}Nd/^{144}Nd$ occurring at 91°-92°W. As argued by these authors, these results require variation in the contribution of at least two mantle source components along axis, with the higher $^{87}Sr/^{86}Sr$ and lower $^{143}Nd/^{144}Nd$ source components increasing to the east. Unraveling the relative contributions from variable melting of variable sources is a long-standing problem in petrology and geochemistry.

Along with the incompatible trace element and isotopic variations are variations in SiO_2, Al_2O_3, FeO and CaO all of which occupy principal lattice sites in the major mantle minerals olivine, pyroxenes, spinel, and garnet. As such, variations in these oxides are more likely to be controlled by stoichiometry during melting than by source enrichment. It is notable that many of the chemical characteristics of the most plume-

influenced portion of the GSC are consistent with relatively low extents of partial melting. For example, E-MORBs are enriched in incompatible elements, and this enrichment is coupled to high Al_2O_3 and low SiO_2 and CaO/Al_2O_3, a feature previously noted by *Langmuir et al* [1992]. The E-MORB lavas, which carry the strongest signature of relatively low extents of melting, are, however, found in the region of shallowest depths and greatest crustal thickness [*Detrick et al*, 2002] and are nearest to the Galapagos "hotspot". Recent studies [e.g., *Plank and Langmuir*, 1992; *Detrick et al*, 2002; *Asimow and Langmuir*, 2003] have suggested that a key to understanding the apparent paradox—maximum melt production (thickest crust) coinciding with low mean extents of melting—is in the role of water on the melting of upwelling mantle peridotite.

By depressing the solidus [*Kushiro*, 1968], the presence of water in the mantle increases the depth at which melting begins, and expands the volume of mantle undergoing melting [*Schilling et al.*, 1980; *Plank and Langmuir*, 1992] (Figure 7). The total melt volume therefore includes a contribution from anhydrous melting, plus a contribution from an additional large volume of mantle undergoing hydrous melting. Because the extent of melting within the hydrous melting zone is likely to be low [*Hirth and Kohlstedt*, 1996, *Hirschmann et al.*, 1999, *Braun et al.*, 2000, *Asimow and Langmuir*, 2003; *Asimow et al.*, 2003], this "extra" source volume can contribute melt with a high proportion of incompatible elements. The total area over which melting takes place and the total melt production are increased, but the mean extent of melting for the total melt volume is reduced. *Gaetani and Grove* [1998] showed that the presence of excess water dissolved in a melt also affects the major element composition of a melt: increasing H_2O decreases SiO_2, FeO, MgO, and CaO.

The recognition of the potential importance of water to enhancing melt production was first noted for the Galápagos region by *Schilling et al.* [1982] and *Fisk et al.* [1982] and also for the region around the Azores hotspot [*Schilling et al.*, 1980; *Bonatti*, 1990; see also *Asimow and Langmuir*, 2003]. In order to understand the relative roles of source composition and variations in melting processes in controlling compositional variation along the GSC, we have developed a quantitative hydrous melting model.

4.1. Theory

Plank and Langmuir [1992] (hereafter *PL92*) evaluated the geochemical effects on crustal composition that are produced by melting and by mixing of melts by examining the residual melting column (RMC, Figure 7a), the conceptual "net result" of melting of the mantle [see *Langmuir et al*, 1992, and *PL92*]. The RMC is useful for calculating the volume and composition of the aggregate melt that makes up the oceanic crust, somewhat independent of the physical shape of the melting region.

When the rate of material flow exiting the melting region is constant over the depth of the melting zone, the width of the RMC is constant and the composition of an aggregate melt derived from different degrees of partial melting (F) from the RMC is calculated by

$$\overline{C_L} = \frac{\int_0^{F\,\max} F[C_L(F)]dF}{\int_0^{F\,\max} FdF}, \qquad [1]$$

where $\overline{C_L}$ is the mean concentration of a given element in the total mass of melt produced by an amount of melting, designated as F (melt fraction). The quantities $\overline{C_L}$ and F are related by a melting function. *PL92*, for example, used the accumulated fractional melting (AFM) equation of *Shaw* [1970],

$$C_L/C_0 = \frac{1-(1-F)^{1/D}}{F}, \qquad [2]$$

where D is the bulk solid/liquid partition coefficient of the element being evaluated, C_0 is the initial source concentration of that element, and fractional melts are pooled between melt fractions 0 and F.

Substituting [2] into [1] and integrating yields the "pooled melting" equation:

$$\overline{C_L}/C_0 = \frac{F_{max} + \frac{(1-F_{max})^{1/D+1} - 1}{1/D+1}}{\frac{F_{max}^{\ 2}}{2}}. \qquad [3]$$

The mean fraction of melting, $\overline{F}$, is the total quantity of melt produced over the height of the melting zone, h_D, divided by the thickness of mantle that has melted over that same interval,

$$\overline{F} = \frac{\int_{h_D}^{0} F(z)dz}{\int_{h_D}^{0} dz}. \qquad [4]$$

where dz is an infinitely small depth interval, and melting begins at h_D, the maximum depth of the melting region, and continues to a depth of zero. Because productivity, B, is $\frac{dF}{dz}$, then for a melting region with constant productivity,

$$\overline{F} = \frac{\int_{h_D}^{0} Bzdz}{\int_{h_D}^{0} dz}. \qquad [5]$$

PL92 approximated B and RMC width as constant, in which case equation [4] reduces to

$$\overline{F} = \tfrac{1}{2} F_{\max}. \qquad [6]$$

Crustal thickness, Z_{cr}, which is proportional to the total volume of melt extracted from the melting region, is calculated simply by multiplying $\overline{F}$ by h_D, the depth to the solidus. Equations [3] and [6] correspond with *PL92* equations [7] and [8], respectively. *PL92* demonstrated that the shape of the melting region could vary significantly and still produce the same RMC. Because C_L/C_0 is calculated from properties of the RMC, melting regions of many shapes lead to predictions of the same pooled melt

compositions. This result is based on four assumptions: passive upwelling, adiabatic melting, perfect fractional melting, and a linear melting function (e.g., constant productivity).

Building upon this previous work, we now relax the assumptions of passive mantle upwelling and constant melt productivity (Figure 7b). In this case, at each depth (z), the RMC width is controlled by $U(z)$, the horizontal flow out of the melting region. The flux of melt removed at a given depth is $U(z)F(z)dz$; the mass flux of a given element is $C_L(z)U(z)F(z)dz$, and therefore adding all melt concentrations from all depths in the RMC yields

$$\overline{C_L} = \frac{\int_{h_W+h_D}^{0} U(z)F(z)C_L(z)dz}{\int_{h_W+h_D}^{0} U(z)F(z)dz}. \qquad [7]$$

This is similar to equation [1], above, but here we integrate over depth range, and we include $U(z)$. The denominator of this equation is the total quantity of mantle exiting the melting region per unit time (i.e., RMC area). For mantle flow that is passively driven by plate separation, $U(z)$ is approximately constant and proportional to the spreading rate of the ridge, and therefore is eliminated from the equation.

We distinguish between the hydrous and anhydrous melting zones by assuming two productivities, B_w and B_D, respectively, that differ from each other but are constant within each melting zone. Water increases the depth at which melting begins by an

amount h_w (Figure 7) and causes melting to a degree F_w before the residue begins to melt at the dry solidus. We also simulate differences in the average upwelling rate between the two zones by allowing the horizontal flow out of the melting zone to differ between the hydrous and anhydrous melting zones: U_w is the uniform flow rate out of the hydrous zone; U_0 is the uniform flow rate out of the dry melting zone. Describing the properties of the two regions separately allows us to simulate much lower productivities [*Hirth and Kohlstedt*, 1996; *Gaetani and Grove*, 1998; *Hirschman et al*, 1999; *Asimow et al.*, 2001] as well as possibly much more rapid mantle upwelling [*Ito et al.*, 1999] in the hydrous zone compared to the anhydrous melting zone. With these assumptions, an equation describing pooled melt concentrations,

$$\overline{C_L}/C_0 = \frac{\frac{1}{C_0}\left[\int_0^{Fw}\frac{U_w F C_L(F)dF}{B_w} + \int_{Fw}^{F\max}\frac{U_0 F C_L(F)dF}{B_D}\right]}{\int_0^{Fw}\frac{U_w F dF}{B_w} + \int_{Fw}^{F\max}\frac{U_0 F dF}{B_D}}, \qquad [8]$$

has two parts. The first integral in the numerator represents melting in the hydrous zone and the second integral in the numerator represents melting in the anhydrous region, which continues to F_{max}, the maximum degree of melting.

With $B_w = \frac{F_w}{h_w}$ [9] and $B_D = \frac{F_{\max} - F_w}{h_D}$, [10]

and using the AFM function [3] to relate C_L to F, we integrate [8] and get our "hydrous melting equation",

$$\overline{C_L}/C_0 =$$

$$\frac{\frac{U_w}{U_0}\frac{h_w}{F_w}\left[F_w + \frac{(1-F_w)^{1/D+1} - 1}{1/D+1}\right] + \frac{h_D}{F_{\max} - F_w}\left[F_{\max} - F_w + \frac{(1-F_{\max})^{1/D+1} - (1-F_w)^{1/D+1}}{1/D+1}\right]}{\frac{U_w}{U_0}\frac{F_w h_w}{2} + \frac{h_D(F_{\max} + F_w)}{2}} \qquad [11]$$

Note that if $F_w = h_w = 0$, [12] reduces to [3], the pooled, anhydrous melting equation of *PL92*.

Mean degree of melting, $\overline{F}$, is the weighted average of the mean degree of melting in the hydrous region and the mean degree of melting in the anhydrous region

$$\overline{F} = \frac{\int_{h_W + h_D}^{0} U(z)F(z)dz}{\int_{h_W + h_D}^{0} U(z)dz} = \frac{\frac{U_w}{U_0}\frac{F_w h_w}{2} + \frac{h_D(F_{\max} + F_w)}{2}}{\frac{U_w}{U_0}h_w + h_D}. \qquad [12]$$

4.2. General Predictions of Hydrous Melting Model

Figure 8 demonstrates the effects of incorporating a hydrous melting region in melting equations, compared to "dry" melting using the pooled melting equation of *PL92*. As h_w increases with increasing concentrations of H_2O in the mantle source, $\overline{F}$ decreases

(Figure 8a). This reflects a relatively large volume of mantle melting to small degrees. Increasing h_w increases the volume flux of low degree melts. Another parameter that increases the flux of material melting in the hydrous region is our active upwelling parameter, U_w/U_0. Increasing U_w/U_0 leads to decreases in $\overline{F}$ at the same value of h_w (Figure 8a).

Figure 8b shows the effects of h_w, B_w, and U_w/U_0 on the enrichment of an incompatible element (D=0.01 shown) in a melt, compared to that predicted by the pooled melting equation for anhydrous, passive upwelling. At very low total degrees of melting, $F_{max} \leq F_w$, and melting is only occurring in the hydrous region. The maximum enrichment is therefore controlled by the h_w and B_w conditions of the hydrous region. While $F_{max} \leq F_w$, C_L/C_0 (for an element modeled with constant D) follows the same curve for all conditions, including anhydrous melting. When productivity increases (i.e., as soon as $F_{max} > F_w$), C_L/C_0 remains higher than the curve for anhydrous melting, because proportionally less "depleted" melts are diluting the concentrations. Lower B_w and h_w values allow more enrichment at very low degrees of partial melting. At higher degrees of melting, e.g. F ≈0.20, melt enrichment is dominated by the upwelling rate (U_w/U_0). At constant B_w, increasing the solidus depression by 20 km (e.g., changing h_w from 30 to 50) has the same effect as doubling the amount of active upwelling (U_w/U_0=1 to U_w/U_0=2). For a very small region of partial melting (h_w=10 km), the enrichment of an element in the melt becomes diluted at high degrees of partial melting (>0.15), and can be nearly approximated by the pooled melting equation [3].

4.3. Application to G' data

An important constraint in our model comes from the crustal thickness measurements that have been made at various locations along the ridge [*Canales et al.*, 2002]. The denominator of equation [11] is proportional to crustal thickness (Z_{cr}). The first and second terms in the denominator are the contributions to the crustal mass by hydrous melting and anhydrous melting, respectively. Known values of Z_{cr} can be incorporated into [11] by substituting

$$F_{max} = \frac{2 * \left[\left(\frac{\rho_c}{\rho_m} * Z_{cr} \right) - \frac{U_w}{U_0} \frac{F_w h_w}{2} \right]}{h_D} - F_w, \qquad [13]$$

where the ratio of crustal density (ρ_c) to mantle density (ρ_m) converts weight fraction to volume fraction.

Other important data from the G' project are our average compositional data for lavas at three different regions along the ridge. Because the processes controlling major element oxides such as SiO_2, CaO, Al_2O_3, and FeO* are not easily accounted for by simple distribution coefficients, we incorporate the incompatible elements K, Na_2O, Ti, and H_2O into our model. The behavior of these elements during melting is moderately well known [e.g., *Dixon et al.*, 1988; *Johnson et al*, 1990; *Langmuir et al.*, 1992; *Michael*, 1995; *Niu et al.*, 1996]. Although partitioning relations can be expected to vary with changing temperature, pressure and composition, there are too few detailed data to

allow for a fully quantitative treatment of these effects. We have therefore adopted a common approach of using constant D values throughout the melting process (Table 4).

The hydrous melting equation [11] C_L is dependent on the "independent" variables D, F_{max}, Z_{cr}, B_D, h_D, B_w, h_w, C_0, and U_w/U_0. The Z_{cr} for each portion of the ridge, and the fractionation-corrected values of K, H_2O, Na_2O, and Ti are input into our model as constant, singular variables for each general MORB-type (Table 4). C_L and Z_{cr} are the only variables for which we have data specific to the GSC.

We have constraints on Ds for the elements modeled, as well as B_D and B_w. We consider only B_D values of 0.26-0.53%/km (0.8-1.6%/kbar). These productivities are consistent with (and even more generous than) productivity values used by *Langmuir et al.* [1992] and *McKenzie and Bickle* [1988], and with average productivity in the anhydrous region estimated by *Asimow et al.* [2001] from F vs. pressure curves. We considered a range of B_w values between 0.03-0.05%/km; these values were also estimated from curves in *Asimow et al.* [2001].

Water concentration in the source and the height of the wet melting column are most likely linked by a simple relationship, however, this relationship is not yet well understood. *Hirth and Kohlstedt* [1996] schematically related the depression of the hydrous solidus to depth (and pressure) based on contours of the activity of water in olivine. The hydrous solidi are sub-parallel to the dry solidus; thus the relationship between C_0^{H2O} and h_w is approximately linear. *Bell et al.* [2003] assert that, due to errors in calibration, all estimations of water solubility in olivine to date are underestimates and require upward revision by a factor of 2-4. Using the *Hirth and Kohlstedt* [1996] solidi

locations, but adjusting the associated H_2O-in-olivine values by a factor of 3, we establish an h_w/C_0^{H2O} slope of ~0.25 km/ppm.

The variables F_{max}, h_D, h_w, C_0, *and* U_w/U_0 are unconstrained, but can be related by equations [9], [10], [11], and [13]. We have four equations relating five unknowns, so our problem is inherently underdetermined. There are a number of ways to approach this problem. *Asimow and Langmuir* [2003] assume C_0 and use forward models to solve for variables F_w (or B_w), F_{max} (or B_D), h_w, and h_D. *McKenzie and O'Nions* [1991] assume C_0 and invert for the same variables. *MacLennan* [2002] builds upon *McKenzie and O'Nions* [1991] to allow for inversion of U_w/U_0. Our approach is to solve for C_0. We use a grid search method to explore the range of C_0, h_D, and U_w/U_0 that acceptably satisfy data on C_L, Z_{cr}, and D given ranges of B_D, B_w, and h_w/C_0^{H2O} that are constrained with laboratory experiments.

5. Results

5.1. N-MORBs

Figure 9a shows the compositional range of sources that can be melted to create our observed average N-MORB concentrations of K, H_2O, Na_2O, and Ti *and* the observed crustal thickness of 5.7 km in the GSC "N-MORB" region (near 97°W). (See Table 6 for parameters associated with these curves.) Enrichments are measured relative to a "midpoint" N-MORB source composition, chosen because the variables h_w, B_w, and C_0^{Na} are near the median of the values for which reasonable solutions were produced. Passive upwelling, $U_w/U_0 = 1$, is assumed to calculate this midpoint.

First we examine predictions of dry melting only ($h_w = F_w = 0$). Because we consider a range of B_D values, there are a number of possible source compositions (dashed lines in Figure 9). Dry melting requires 41-53 ppm K in the source, 136-175 ppm H_2O, 2100-2600 ppm Na_2O, and 991-1136 ppm Ti. The value of $\overline{F}$ for dry melting ranges from 0.08 to 0.104. Lower B_D values combined with a deep dry solidus (high h_D) require a less enriched source and lower $\overline{F}$ than high productivity over a shorter dry melting column (Table 6). We emphasize that the C_0 values for K, H_2O, and Ti are "controlled" by the C_0^{Na2O}, because the predicted results "match" the observed results when $C_L^{Na}{}_{pred} = C_L^{Na}{}_{obs}$. C_0 values for K, H_2O, and Ti are calculated using the set of variables that produced the match. Thus, the range of acceptable C_0 for these incompatible elements is controlled by the range of C_0^{Na2O} values that produce reasonable solutions.

In comparison to the dry melting solutions, when a hydrous melting component is factored in, our N-MORB data can be reproduced with *lower* incompatible element concentrations in the source at lower values of $\overline{F}$. Using the hydrous melting equation, N-MORB compositions can be produced from a source with as little as 26 ppm K, 107 ppm H_2O, 1900 ppm Na_2O, and 955 ppm Ti, and $\overline{F}$ as low as 0.046. This low $\overline{F}$ solution is created by 26 km of wet melting with $B_w = 0.04\%$/km and $U_w/U_0 = 2$, plus 54 km of dry melting with $B_D = 0.27$ %/km. Hydrous melting 36 km deep with $B_w =$ 0.03%/km and $U_w/U_0 = 1$ plus 41.5 km dry melting with $B_D = 0.49$ %/km requires the *maximum* source concentration: 35 ppm K, 141 ppm H_2O, 2400 ppm Na_2O, and 1113 ppm Ti. Concentrations between these extreme values are also viable, but created by different combinations of the above variables.

These N-MORB results elucidate the importance of an equation that can account for the effects of H_2O present in the mantle. The hydrous melting equation produces N-MORB solutions with *lower* average degrees of melting than the anhydrous pooled melting equation, thus reducing the required concentrations of the incompatible elements in the mantle source *and* the required temperature of the mantle.

5.2. E-MORBs and T-MORBs

In evaluating the E-MORB and T-MORB data, we consider several important questions. Is an enriched mantle in the E-MORB region *required* to explain basalt compositions that are incompatible- element- enriched relative to N-MORBs? Is an active upwelling component required? What are the effects of variable productivities within the hydrous melting region? What is the additional depth to the hydrous solidus? Must E-MORBs be produced by elevated mantle temperatures (roughly proportional to h_D) relative to N-MORBs?

Figure 9 compares the maximum and minimum source enrichments required of each MORB-type for solutions to both hydrous and anhydrous equations. All solutions are normalized to the source values for the N-MORB "midpoint". E-MORB solutions span a large range of possible source enrichments that encompasses nearly the entire range of N-MORB solutions. Many, but not all, of the E-MORB solutions require a more enriched source than for N-MORB. T-MORB solutions span a range that includes solutions with both higher *and* lower source concentrations than the maximum and minimum N-MORB solutions, respectively, although T-MORB maximum values for H_2O, Na_2O, and Ti are only very slightly greater than N-MORB maximum values.

Parameters corresponding with each of the lines plotted on Figure 9 are reported in Table 6.

The required source concentration depends strongly on the upwelling rate (Figure 10). The more material that is cycled through the hydrous melting region relative to the anhydrous melting region (i.e., U_w/U_0), the less source enrichment is required. This dependence on upwelling rate is strongest for the most incompatible element, K. The K level in the E-MORBs can be produced from N-MORB source compositions only at very high upwelling rates ($U_w/U_0 \geq 10$). T-MORBs require a source enriched in K relative to N-MORBS only at lower upwelling rates ($U_w/U_0 \leq 3$). Neither T-MORBs nor E-MORBs *require* Na-enrichment, although at low upwelling rates some T- and E-MORB solutions have lower Na contents than N-MORBs. At high upwelling rates ($U_w/U_0 \geq 5$) some E- and T-MORB solutions require sources with *less* Na than N-MORBs. E-MORBs require at least some Ti-enrichment; there are no solutions at any U_w/U_0 that match N-MORB source Ti values. The Ti content of the T-MORB source does not vary significantly from that of the N-MORB source. The required source concentration also depends upon B_w. The more "productive" the hydrous melting region, the less source enrichment is required, for the range of B_w between 0.03 and 0.05 %/km (Figure 10).

The relationship between source H_2O and $\overline{F}$ is shown in Figure 11a. The model allows E-MORB mantle to contain as little as ~110 ppm H_2O or as much as ~237 ppm, compared to between 107 and 141 ppm H_2O in our N-MORB mantle and 77 – 146 ppm in our T-MORB mantle. Mean degree of melting for E-MORBs may be anywhere from 0.019 to 0.062, depending on the upwelling rate and productivity in the hydrous region (B_w). N-MORB $\overline{F}$, by comparison, could range from 0.046 to 0.062, and T-MORBs

could range from 0.021 to 0.069. $\overline{F}$ is dominantly controlled by the upwelling rate. Figure 11b shows that if indeed E-MORBs are created by lower $\overline{F}$ than N-MORBs, as inferred from SiO_2, and CaO/Al_2O_3 values, there must be some active upwelling component in the E-MORB region.

The range of possible values of h_D, depth to the dry solidus, for N-, T-, and E-MORBs is shown in Figure 12. Larger B_D values couple with smaller (shallower) h_D values to match our data. B_D—a result of our model, not an input—is calculated from F_{max} and F_w, which together incorporate the Z_{cr} value for that portion of the ridge and the input variables h_w, U_w/U_0, and B_w. The value of h_D depends on the combination of these variables; plots of h_D versus any one of them are inadequate.

The B_D values we allowed as viable solutions (0.27 – 0.53 %/km, or ~0.8-1.6%/kbar) limit the maximum and minimum h_D values. E-MORB solutions are between 41.5 and 54 km depth to solidus; T-MORB solutions range from 42 to 49.5 km, and N-MORBs range from 45 to 51.5 km. Figure 12 shows that for similar B_D values, the depth to solidus difference (Δh_D), and therefore the temperature difference (ΔT), between N-MORBs and E-MORBs is quite small. Δh_D can be converted to ΔT using the slope of the mantle solidus. For simplicity, we use a linear relationship, which we derived by fitting a line to the not-quite-linear solidus of *Hirschmann* [2000]. We use a relationship of 3.8°C/km. At any given B_D value, the maximum Δh_D between N-MORB and E-MORB solutions is 9 km, or ~34°C. When similar B_w values are compared between N- and E-MORB regions, this difference reduces to as little as 3 km, or ~11°C. T-MORB depths and temperatures are very similar to those for the N-MORBs. Thus, our model indicates that the Galápagos "hotspot" increases the temperature of the mantle beneath the inflated

portion of the GSC by only a few tens of degrees relative to our model N-MORB mantle, and this temperature difference is restricted to the E-MORB region alone; i.e., there is no mantle thermal anomaly required west of 92.7°W.

5.3. Role of the Relationship between h_w and C_0^{H2O}

Because the relationship between water content in the mantle source and the mean degree of melting is a key result of our model, it is important to understand the effect of the value chosen to represent the relationship between water content and the depression of the solidus (h_w and C_0^{H2O}). Our C_0^{H2O} values have been calculated to match the observed fractionation-corrected H_2O values in basalts erupted along the GSC and the average crustal thickness for that region. These values will not change significantly regardless of the relationship between h_w and C_0^{H2O} used. The range of h_w values that can couple with C_0^{H2O} *is* limited by this relationship.

Reducing h_w/C_0^{H2O} to a value similar to that used by *Asimow and Langmuir* [2003] (~0.05 km/ppm) will decrease the h_w associated with calculated C_0^{H2O}, thus decreasing the relative contribution of the hydrous melting zone to the total area over which melting occurs. Consequently, $\overline{F}$ solutions will shift to higher values, although only ~0.01 for the entire range. Increasing the h_w/C_0^{H2O} slope to a value like that estimated from *Hirth and Kohlstedt* [1996] *without* the adjustment for water solubility in olivine of Bell et al. [2003] (i.e., h_w/C_0^{H2O} ~0.45-0.5 km/ppm) causes the range of solutions to shift to lower $\overline{F}$ values (again, though, only by ~0.01 total). By contrast, if a change in h_w/C_0^{H2O} is coupled with a change in the estimated B_w such that the relationship between h_w and F_w remains the same, our $\overline{F}$ results are unchanged. It is important to

better quantify the effect of H_2O in the mantle on the depression of the solidus through future research, but the relationship between h_w and $\overline{F}$ should not change.

6. Discussion

6.1. Most Likely Solutions for G' Data

In order to assess the full range of potential solutions to our G' data, we have allowed a generous range of variables. However, we may reasonably constrain our results further in an attempt to produce most-likely solutions for the different regions of the GSC. Solutions were eliminated using the following logic.

(1) Average productivity in the wet region (B_w) for E-MORBs is likely to be greater than or equal to B_w in the N-MORB region. We eliminated $B_w > 0.03$%/km in the N-MORB region; all B_w values were allowed in the T- and E-MORB regions.

(2) Crustal thickness, axial morphology, and the N-MORB composition are typical of normal mid-ocean ridge basalts globally; therefore we may infer that the N-MORBs were created by passive upwelling. We allowed only N-MORB solutions for $U_w/U_0 = 1$. Similarly, thicker crust and inflated axial morphology in the E-MORB region indicate that at least some additional material is making its way to the ridge [*Canales et al.*, 2003]; thus we eliminated E-MORB solutions created by passive upwelling ($U_w/U_0 = 1$).

(3) We expect relatively constant average productivity in the anhydrous region beneath the ridge. We narrowed our generous B_D range to between 1.2 and 1.4%/km [*Asimow et al.*, 2001, Figure 4c, curve 2] for all MORB types.

(4) Although some enrichment in the incompatible elements in the E-MORB and T-MORB regions may be necessary to explain the data, it is unlikely that the plume-

affected region(s) are *depleted* in these elements relative to the N-MORB region. Thus, we eliminated any T- or E-MORB solutions that require source concentrations of Na (our only *input* source concentration) that are less than N-MORB solutions remaining after steps 1-3.

(5) Finally, we assume that the additional zone of hydrous melting is at least as deep in the T- and E-MORB regions as in the N-MORB region. We eliminated any solutions where h_w for the T-MORB or E-MORB source was less than h_w for the N-MORB source.

These additional constraints considerably narrow the range of solutions. They imply that GSC N-MORBs were created by melting of a passively upwelling source with 34±1 ppm K, 133±3 ppm H_2O, 2250±50 ppm Na_2O, and 1050±25 ppm Ti. Mean degree of melting was 0.06±0.005 and the maximum degree of melting was 0.19±0.007 over 33±1 km of wet melting plus 47±2 km of dry melting.

If the T-MORBs were created by any upwelling, it is less than U_w/U_0 =2. Solutions produced by higher U_w/U_0 values were ruled out by restrictions (4) and (5). T-MORB parental magma compositions vary from those for N-MORBs only in the highly incompatible element, K. This variation can be explained by either slightly higher $\overline{F}$ of a source with only a few ppm more H_2O than the N-MORB source (when U_w/U_0 = 1), or slightly lower $\overline{F}$ of a source with a few ppm less H_2O than for N-MORB (when U_w/U_0 = 1.5) (Figure 13). Regardless, our results indicate that T-MORBs can be created by melting a source very similar to the N-MORB source: 49±4 ppm K, 133±9 ppm H_2O, 2300±100 ppm Na_2O, and 1080±30 ppm Ti. T-MORB $\overline{F}$ is 0.061±0.006 and F_{max} is 0.20±0.01; h_w = 34±2 km and h_D = 48±3 km.

The maximum upwelling rate in the E-MORB region allowed by restrictions (4) and (5) is $U_w/U_0 = 3.5$. This limits the minimum $\overline{F}$ of E-MORBs to 0.033, and requires that E-MORBs have at least some K and H_2O source enrichment relative to N-MORBs and T-MORBs. E-MORBs then would have melted from a source with 75±14 ppm K, 185±22 ppm H_2O, 2350±150 ppm Na_2O, and 1430±60 ppm Ti. Accordingly, the depth to the hydrous solidus is deeper in the E-MORB region: $h_w = 46\pm6$ km. The depth to the anhydrous solidus, 50±2 km, is only slightly deeper (and warmer) if at all than h_D for the N- and T-MORB regions.

With these stricter parameters, we can evaluate the conditions that affect the along-axis crustal thickness and glass compositional variability for the GSC. The source for T-MORBs varies only slightly from that for N-MORBs; crustal thickness variations between the two regions can be accounted for with a moderate component of active upwelling ($U_w/U_0 = 1.5$), creating slightly lower $\overline{F}$ and requiring a few ppm less water in the source than for N-MORBs. To create the composition and crustal thickness values observed in the E-MORB region requires a source moderately enriched in incompatible elements combined with an upwelling component (U_w/U_0) > 1 but < 3.5. The production of E-MORBs requires a mantle only slightly warmer (11±11°C) and damper (52±19 ppm H_2O) mantle. The trends in SiO_2 , CaO/Al_2O_3, and FeO contents of the E-MORB glasses are consistent with those predicted by *Gaetani and Grove* [1998] in the presence of excess H_2O

6.2. Global and Local Implications

Even the most "normal" mid-ocean ridges contain some amount of water [*Michael*, 1987; *Dixon et al.*, 1988; *Michael*, 1995; *Danyushevsky et al.*, 2000]. Our equations that take into account the "extra" region—no matter how small or large—of low-degree partial melts contributed by the presence of water have implications for the concept of "typical" degrees of melting at mid-ocean ridges, and for the composition of incompatible-element-depleted mantle from which MORB are generated. Normal mid-ocean ridges are commonly considered to be produced by mean extents of melting of ~ 10% from a melting column on the order of 60 km deep, producing ~ 6 km of crust [e.g., *Klein et al*, 1991; *Langmuir et al.*, 1992; *Forsyth*, 1993].

Recent works by several authors, including the present study, indicate that this 10% value should be reevaluated. We estimate that the GSC N-MORBs were created by ~ 6 % melting. *Forsyth* [1993] and *Plank et al.* [1995], who defined "mean F" as the mean value of F (F_v) for melts pooled from the melting region (as opposed to F_B, bulk melt fraction), concluded that average N-MORBs are produced by ~6.67% melting. *Asimow et al.* [2001] predicted a mean melt fraction of no more than 8% for N-MORBs. Using new (pHMELTS) algorithms, *Asimow and Langmuir* [2003] predict F_B as low as 6.5% for normal regions of the Galápagos Spreading Center and the Mid-Atlantic Ridge near the Azores. It is clear that paradigms are shifting in regards to the mean degree of melting that produces N-MORBs. Additionally, when hydrous melting is accounted for, estimations of the composition of the mantle beneath even "normal" segments of mid-ocean ridges must be reevaluated [*Asimow and Langmuir*, 2003; this study]. Hydrous melting allows the N-MORB source to be even more depleted in incompatible elements than was previously allowed by dry melting equations.

This study documents the major element, geophysical, and bathymetric variability along the axis of the Galápagos Spreading Center, and the effects of the nearby Galápagos plume on the characteristics of the mid-ocean ridge. We show that plume influence is strongest in the region of the GSC that is closest to the hotspot, with peaks near 91.8°W, and that the effects diminish with distance from the plume. We show that only a slight temperature anomaly, coupled with moderately enriched mantle material, can explain the crustal thickness and glass compositional variations in the "enriched" region of the ridge. The exact nature of the Galápagos plume itself, as well as the mechanism for transport and mixing of plume material, is left for future study.

7. Conclusions

1. Samples collected from the GSC can be classified as N-, T-, or E- MORB based on K/Ti ratios > 0.15, 0.15 to 0.09, and < 0.09, respectively. High K/Ti E-MORBs are also characterized by higher H_2O, Al_2O_3, and Na_2O, and lower FeO*, SiO_2, and CaO/Al_2O_3 relative to N-MORBs at similar values of MgO. T- and E-MORBs may be further subdivided into T1, T2, T3, E1, and E2 based on CaO/Al_2O_3 ratios, SiO_2 content, and subtle variations in incompatible elements.

2. E-MORBs dominate the GSC east of 92.6°W, where the crust is thickest (6.5-8 km). T-MORBs are mainly found between 92.6°W and 95.5°W, where crustal thickness is 6-7 km. West of the propagating rift tip at 95.5°W, where crustal thickness is < 6 km, N-

MORBs dominate. E-MORB incompatible element concentrations, including H_2O, peak near 91.8°W and decrease with increasing distance from the hotspot. $Fe_{8.0}$, $Si_{8.0}$, and $Ca_{8.0}/Al_{8.0}$ all show their lowest values near 91.8°W.

3. Geochemical boundaries correlate with geophysical and morphological characteristics. The transition from N-MORBs to T-MORBS occurs at the 95.5°W propagating rift, which also marks the boundary between axial rift-valley morphology and transitional morphology. Near 92.7°W, morphology abruptly changes from transitional to an axial high, the axial magma chamber seismic reflector shoals by >1 km, the thickness of seismic layer 2A diminishes by half, and lavas become dominated by E-MORBs.

4. We have developed a hydrous melting equation that considers the effects of an "additional" zone of hydrous melting that is created by the depression of the mantle solidus in the presence of water in the mantle. Variables in the equation include depth of the additional hydrous melting zone (h_w), the fraction of melt per unit of depth in the hydrous region (productivity, B_w), source enrichment in incompatible elements and H_2O (C_0^i), and the flow rate of material passing through the hydrous region relative to the anhydrous region (upwelling rate, U_w/U_0). We use this hydrous melting equation to model the variables that may combine to match the crustal thickness and concentrations of K, Na_2O, H_2O, and Ti in lavas that we measured along the GSC.

5. Incompatible element concentrations in pooled magmas are predicted to increase with source concentration, height of the hydrous melting zone, and upwelling rate. Of these

variables, upwelling rate has the strongest effect on $\overline{F}$. Higher U_w/U_0 values correspond to lower $\overline{F}$.

6. Using the hydrous melting equation, we estimate the GSC N-MORBs were created by $\overline{F}$ ~0.06 from a source with ~34±1 ppm K, 133±3 ppm H_2O, 2250±50 ppm Na_2O, and 1050±25 ppm Ti. The absolute value of $\overline{F}$ is highly dependent on the poorly constrained effect of small amounts of water on the position of the solidus at highly water-undersaturated (damp) conditions.

7. Higher upwelling rates in the E-MORB region require less source enrichment. The E-MORB region must be enriched in K unless the upwelling rate is > 10. E-MORB $\overline{F}$ may be as low as 0.018 if $U_w/U_0 = 10$, or as high as 0.065 if $U_w/U_0 = 1$.

8. Depending on U_w/U_0 and B_w, the E-MORBs may have as little as 110 ppm H_2O or as much as 237 ppm H_2O. The corresponding depth of this solidus is dependent on the value used to relate h_w and C_0^{H2O}; we estimate h_w in the E-MORB region to be between 28 km and 58 km, using h_w/C_0^{H2O} of 0.025 km/ppm.

9. We estimate a *maximum* ΔT of ~34°C between the N-MORB region and E-MORB region.

10. The crustal thickness and glass compositional variations in the E-MORB-dominated region of the GSC can best be explained by only a slight temperature increase (11±11°C), coupled with a moderately enriched mantle source and upwelling of 1.5-3.5 times passive upwelling rates. The transitional region requires only slight upwelling (U_w/U_0 =1.5) and a source enriched only slightly in K.

Table 1. Location and estimated recovery of all sampling stations[a]

Stn.[b]	Type	Latitude	Longitude	Site	Recovery
1	Dredge	0° 06.2'S	89° 40.9'W	Small seamount on platform	1 Mn-coated rock
2	Dredge	1° 35.3'N	90° 49.0'W	Volcano in transform zone	~120 kg of glassy, aphyric pillow talus
3	Wax Core	1° 53.35'N	90° 59.15'W	Ridge tip near transform intersection	3 g glass
4	Dredge	1° 53.5'N	91° 03.4'W	Ridge axis	~ 50 g glass fragments - lineated sheet lava
5	Wax Core	1° 53.60'N	91° 04.55'W	Ridge axis	2-3 g glass
6	Dredge	1° 54.1'N	91° 10.8'W	Ridge axial high	5 pillow fragments
7	Dredge	1° 55.2'N	91° 16.4'W	Ridge axis	5 kg pillow fragments
8	Wax Core	1° 57.4'N	91° 21.4'W	"Flat" top of volcano	1 g glass + sand
9	Dredge	1° 56.0'N	91° 19.3'W	Axial high	150-200 kg sheet lava
10	Dredge	1° 57.6'N	91° 21.7'W	Flat-topped, big volcano	5-10 kg sheet lava
11	Dredge	1° 58.3'N	91° 24.1'W	Small ridge on axis	5 pillow fragments + 50 g glass
12	Dredge	1° 59.1'N	91° 29.0'W	Small volcano on axial high	100 g glass chips
13	Dredge	2° 00.3'N	91° 33.5'W	S. limb of OSC[c]	5-10 kg aphyric sheet lava
14	Wax Core	2° 01.10'N	91° 36.45'W	Top edge of axial volcano	4 g glass
15	Dredge	2° 02.7'N	91° 36.3'W	N. limb of OSC	150 kg aphyric, vesicular lava
16	Dredge	2° 03.6'N	91° 44.6'W	Axial trough	10 kg Mn-crusted pillow talus
17	Dredge	2° 04.2'N	91° 48.0'W	60 m-high axial volcano	120 kg sheet lava
18	Dredge	2° 06.1'N	91° 52.7'W	Flank of small axial volcano	200 g plag-phyric glass chips
19	Dredge	2° 06.6'N	91° 57.3'W	Large axial volcano	30 kg lobate lava
20	Dredge	2° 06.9'N	92° 00.5'W	N. limb of OSC	60 kg lava fragments
21	Dredge	2° 06.2'N	92° 03.1'W	Small high on axis	5-10 gm glass chips
22	Dredge	2° 06.4'N	92° 09.4'W	End of axial ridge	50 g glass chips
23	Dredge	2° 06.5'N	92° 13.3'W	Narrow ridge tip	4 kg pillows + glass chips
24	Dredge	2° 07.5'N	92° 14.6'W	Tip of N. limb of OSC	1 rock + glass chips
25	Dredge	2° 08.7'N	92° 19.3'W	Axial graben	60 kg of glassy lava + pillar
26	Wax Core	2° 09.5'N	92° 22.35'W	Top of axial hill	25 g glass
27	Dredge	2° 10.2'N	92° 25.6'W	Axial ridge	5-10 g glass
28	Dredge	2° 11.2'N	92° 31.2'W	Local high at segment end	2 pillow fragments + glass
29	Dredge	2° 12.1'N	92° 37.1'W	Narrow axial ridge	120 kg aphyric lava
30	Dredge	2° 13.4'N	92° 41.7'W	40 m-high volcano	~50 g glass shards
31	Dredge	2° 14.6'N	92° 49.3'W	Axial deep	10 kg rock + glass
32	Dredge	2° 16.1'N	92° 52.9'W	Volcanic mound in axis	2 pillow fragments with glass
33	Dredge	2° 16.9'N	92° 58.4'W	Axial graben	6 kg pillow fragments
34	Dredge	2° 17.4'N	93° 00.6'W	Axial graben	2 kg fresh, glassy ol+pl[c] basalt
35	Dredge	2° 18.0'N	93° 02.9'W	Axial graben	10 kg ol+pl pillow basalt
36	Dredge	2° 26.6'N	93° 25.9'W	S. flank of axial volcano	~200 g glassy chips
37	Dredge	2° 23.6'N	93° 21.2'W	Small volcano in axis	500 g glass shards
38	Dredge	2° 21.4'N	93° 16.1'W	N. side of axial deep	Several rock fragments + glass
39	Dredge	2° 20.5'N	93° 13.1'W	Axial graben	< 1 kg glass chips
40	Dredge	2° 19.5'N	93° 09.5'W	Small volcano in graben	8 kg pl+ol sheet flow fragments
41	Dredge	2° 18.8'N	93° 05.6'W	N. side axial deep	150 kg big pillow fragments
42	Dredge	2° 23.5'N	93° 12.3'W	E. tip of N. limb of OSC	~200 g pillow fragment + glass
43	Dredge	2° 24.7'N	93° 15.3'W	Bump on ridge axis	2 kg pl+ol sheet flow fragments
44	Dredge	2° 25.2'N	93° 17.7'W	Axial deep	200 g glass chips
45	Dredge	2° 26.6'N	93° 21.1'W	Volcano in graben	20-25 kg pillows + glass
46	Dredge	2° 27.2'N	93° 29.5'W	Small bump in axis	Glass fragments

Table 1. Location and estimated recovery of all sampling stations[a]

Stn.[b]	Type	Latitude	Longitude	Site	Recovery
47	Dredge	2° 27.8'N	93° 33.7'W	Volcano in graben	One rock + glass
48	Dredge	2° 29.3'N	93° 39.3'W	Small high in graben	~2 kg pillows + glass
49	Dredge	2° 30.0'N	93° 52.1'W	Small ridge on axial high	5 kg rock + sediment + shrimp
50	Dredge	2° 30.0'N	93° 46.5'W	N. flank of axial volcano	70 kg altered pillows (ol+pl)
51	Dredge	2° 30.6'N	93° 57.7'W	Small rise in axial trough	< 1 kg glassy, pl-phyric rock
52	Dredge	2° 30.2'N	94° 03.6'W	Axial pit	< 100 g glass
53	Dredge	2° 30.5'N	94° 07.6'W	Deep, maybe off axis	10-15 kg mud + pillow fragments
54	Wax Core	2° 32.3'N	94° 10.3'W	Top of ridge	2 g aphyric glass
55	Dredge	2° 32.0'N	94° 13.1'W	Flank of axial volcano	~100 g glass + sheet fragments
56	Dredge	2° 33.2'N	94° 14.3'W	Ridge on axial high	200 kg pl+ol pillows
57	Dredge	2° 32.2'N	94° 16.4'W	Irregular axial bump	200 g aphyric glassy rinds
58	Dredge	2° 31.6'N	94° 20.9'W	1 km volcano; south side of axis	150 kg porphyritic pillow basalt
59	Dredge	2° 32.5'N	94° 25.9'W	Volcano on south side of graben	10 kg plag-phyric glassy pillows
60	Dredge	2° 34.3'N	94° 35.9'W	High in axial graben	25 kg pl-phyric glassy buds
61	Dredge	2° 33.8'N	94° 32.2'W	Local high in axial graben	1-2 kg of pillow fragments + glass
62	Dredge	2° 34.9'N	94° 39.6'W	Bump in center of graben	75 kg big, pl-phyric pillows
63	Dredge	2° 35.5'N	94° 44.7'W	Volcano in axial graben	500 g pl-phyric glass pieces
64	Dredge	2° 36.0'N	94° 49.1'W	Axial rise structure	200 kg pl+ol pillows
65	Dredge	2° 36.6'N	94° 54.4'W	Axial volcano	1.5 kg rock + glass
66	Dredge	2° 36.9'N	94° 58.6'W	Axial high in graben	150 kg pl-phyric pillows
67	Dredge	2° 37.6'N	95° 01.9'W	Big axial volcano	120 kg large pillows
68	Dredge	2° 37.0'N	95° 08.4'W	Rise in axis	80 kg aphyric pillows
69	Dredge	2° 38.1'N	95° 12.6'W	High in axial valley	20 kg aphyric sheet fragments
70	Dredge	2° 37.8'N	95° 18.9'W	Narrow axial ridge	25 kg ol+pl pillows and sheets
71	Dredge	2° 25.3'N	95° 36.1'W	Ridge in North Graben	30 kg pillow fragments
72	Wax Core	2° 25.3'N	95° 37.2'W	Ridge in North Graben	4 g glass
73	Dredge	2° 17.9'N	95° 42.0'W	Mound in axial graben	1 kg plag-phyric lava
74	Dredge	2° 17.9'N	95° 47.5'W	Small volcano in graben	30 g plag-phyric glass chips
75	Dredge	2° 17.7'N	95° 52.5'W	Base of south wall of graben	250 g pl+ol-phyric glass chunks
76	Dredge	2° 17.4'N	96° 07.4'W	Irregular volcano	300 g porphyritic glass chunks
77	Dredge	2° 16.8'N	96° 11.4'W	Small volcano caldera	<1 kg pl-phyric rock + glass
78	Dredge	2° 18.9'N	96° 19.8'W	Small volcano in valley	<50 g sediment + glassy scoria
79	Dredge	2° 05.9'N	96° 43.4'W	Small volcano in graben	30 kg pl-phyric pillows
80	Dredge	2° 06.8'N	96° 37.7'W	Small volcano in valley	10 kg pl-phyric pillows and sheets
81	Dredge	2° 07.1'N	96° 41.7'W	Volcano	70 kg hydrothermally altered pl-phyric pillows
82	Dredge	2° 07.2'N	96° 46.5'W	Volcano	100 kg pl-phyric pillows
83	Dredge	2° 08.1'N	96° 49.0'W	Small axial volcano	30 kg sheet lava
84	Dredge	2° 08.2'N	96° 52.5'W	Elongate axial volcano	10 kg pl-phyric pillows
85	Dredge	2° 09.2'N	96° 57.6'W	Axial volcano in graben	100 g pl-phyric glass
86	Dredge	2° 08.1'N	96° 59.7'W	Medium axial volcano	150 g pl-phyric glassy pillows
87	Dredge	2° 08.2'N	97° 05.9'W	Volcano flank in axis	20 kg pl-phyric sheets and pillows
88	Dredge	2° 08.4'N	97° 11.5'W	Circular volcano	45 kg pl-phyric pillows

Table 1. Location and estimated recovery of all sampling stations[a]

Stn.[b]	Type	Latitude	Longitude	Site	Recovery
89	Dredge	2° 08.0'N	97° 21.4'W	Volcanic ridge	50 g glass
90	Wax Core	2° 07.1'N	97° 15.5'W	Side of ridge in graben	2 flecks of glass
91	Dredge	2° 08.5'N	97° 36.2'W	Volcano on ridge	150 kg hydrothermally altered pillows and sheets
92	Dredge	2° 11.5'N	97° 46.9'W	Irregular volcano	200 kg sheets and pillows

[a]Recovery estimations were made at sea.

[b]Dredge or wax core station number

[c]OSC, Overlapping Spreading Center

[d]ol, olivine; pl, plagioclase

Table 2. Major element and H_2O data[a]

Group[b]	MORB-Type[c]	SiO_2	TiO_2	Al_2O_3	FeO	MgO	CaO	Na_2O	K_2O	P_2O_5	Total	K/Ti	Mg#[d]	H_2O	Sample number[e]
2D	N	49.5	0.81	15.8	9.71	9.24	12.72	1.72	0.03	0.05	99.8	0.049	62.9	0.075	2D-1
3C	E	49.7	1.89	13.7	12.76	6.40	11.06	2.64	0.21	0.17	98.8	0.157	47.2		
4D	T3	49.1	1.50	15.5	10.19	7.99	12.22	2.51	0.12	0.13	99.4	0.115	58.3	0.248	4D-1
5C	E	49.7	1.85	14.1	11.61	6.79	11.56	2.66	0.21	0.16	98.9	0.159	51.1		
6D	T	50.1	1.41	14.4	11.13	7.54	12.16	2.33	0.11	0.11	99.5	0.112	54.7		
7D-a	E	49.8	1.87	14.3	11.69	6.79	11.31	2.71	0.23	0.18	99.1	0.173	50.9	0.400	7D-4
7D-b	T3	49.2	1.80	14.8	10.76	7.22	12.05	2.75	0.18	0.15	99.1	0.136	54.5	0.341	9D-1.1
8C	E	50.0	2.75	13.3	13.86	5.00	9.27	3.04	0.48	0.31	98.2	0.240	39.1		
9D-a	T3	49.7	1.88	14.3	11.49	6.93	11.58	2.72	0.17	0.15	99.2	0.128	51.8		
9D-b	T3	49.2	1.64	15.4	10.44	7.76	11.86	2.61	0.15	0.13	99.4	0.123	57.0		
10D	E	50.3	2.83	13.3	13.98	4.88	9.32	2.98	0.49	0.32	98.6	0.239	38.4	0.722	10D-1
11D-a	E	53.2	2.57	13.2	13.26	3.33	7.43	3.28	0.82	0.51	97.9	0.440	30.9	1.077	11D-1
11D-b	E	51.7	2.95	13.1	14.04	3.98	8.14	3.25	0.71	0.50	98.7	0.333	33.5		
12D	E	50.4	2.98	12.9	14.46	4.60	8.88	3.07	0.51	0.39	98.4	0.237	36.2	0.793	12D-5
13D	E	50.0	2.90	13.3	13.64	4.90	9.34	2.93	0.57	0.39	98.2	0.271	39.0		
14C	E	50.4	3.21	12.5	15.20	4.20	8.51	2.85	0.52	0.41	98.1	0.223	33.0		
15D	T2	49.6	1.49	14.8	10.35	8.02	11.85	2.20	0.17	0.15	98.8	0.161	58.0	0.304	15D-1
16D	E2	48.2	2.16	15.7	10.65	6.77	10.85	3.10	0.31	0.25	98.2	0.200	53.1	0.574	16D-2
17D-a	E2	47.6	2.00	16.7	9.43	7.20	10.99	3.32	0.38	0.27	98.1	0.264	57.6	0.612	17D-4
17D-b	E2	47.6	1.93	16.9	9.28	7.63	10.96	3.25	0.36	0.25	98.3	0.255	59.4		
18D	E	49.0	1.57	15.0	10.06	7.54	12.04	2.56	0.23	0.17	98.4	0.198	57.2		
19D	E	50.4	2.73	13.4	13.62	4.79	9.08	3.24	0.47	0.34	98.3	0.240	38.6	0.819	19D-1
20D-a	E2	48.1	1.63	16.6	9.60	8.14	11.85	2.59	0.27	0.18	99.1	0.225	60.2		
20D-b	E2	48.6	1.73	16.2	9.80	7.72	11.74	2.75	0.29	0.20	99.1	0.231	58.4	0.441	20D-1
21D	E	49.3	2.06	14.6	11.21	6.51	11.16	3.01	0.32	0.21	98.5	0.212	50.8		
22D	E	49.3	2.24	14.7	10.85	6.45	11.72	3.09	0.41	0.27	99.2	0.254	51.5		
23D	E	49.9	1.86	14.2	11.46	6.52	11.28	2.74	0.26	0.18	98.6	0.194	50.4		
24D	E	49.8	1.84	14.6	10.75	6.98	11.45	2.55	0.26	0.20	98.6	0.193	53.6		
25D-a	E	49.6	1.63	15.1	10.17	7.17	11.90	2.54	0.27	0.18	98.7	0.233	55.7	0.383	25D-1
25D-b	E	49.4	1.61	15.0	10.20	7.55	11.83	2.52	0.26	0.16	98.8	0.226	56.9		
26C	E	50.0	1.67	14.8	10.17	6.83	11.39	2.59	0.48	0.20	98.3	0.402	54.5		
27D	E	50.2	2.06	13.6	12.63	6.14	10.66	2.50	0.22	0.20	98.4	0.151	46.4		
28D	E	50.2	1.57	14.3	10.89	7.08	11.90	2.41	0.22	0.14	98.9	0.189	53.7	0.328	28D-1
29D	T	50.4	1.67	13.9	11.80	6.84	11.24	2.42	0.16	0.14	98.8	0.135	50.8	0.301	29D-1
30D	E	50.3	2.13	13.2	13.45	5.81	10.29	2.59	0.23	0.21	98.5	0.149	43.5		
31D	T	50.1	1.82	13.7	12.50	6.42	10.83	2.63	0.18	0.15	98.5	0.135	47.8		
32D	T	50.3	1.66	13.7	12.40	6.79	11.07	2.21	0.14	0.14	98.5	0.118	49.4		
33D	T	50.4	1.61	13.7	12.57	6.72	10.89	2.32	0.14	0.13	98.7	0.123	48.8	0.269	33D-1
34D-a	T	50.2	1.49	14.2	11.47	7.22	11.74	2.24	0.13	0.12	99.1	0.122	52.9		
34D-b	T	50.5	1.53	14.1	11.72	7.08	11.69	2.34	0.13	0.14	99.5	0.120	51.9		
35D-a	T	50.6	1.74	13.8	12.53	6.50	11.16	2.54	0.14	0.15	99.4	0.112	48.1		
35D-b	T	50.8	1.81	13.5	12.82	6.40	11.17	2.59	0.15	0.15	99.6	0.113	47.1		
36D	T	50.8	1.57	14.1	11.77	7.06	11.33	2.34	0.15	0.16	99.5	0.130	51.7		
37D	T	50.9	1.33	14.3	11.16	7.32	12.07	2.25	0.11	0.11	99.8	0.116	53.9		
38D	T	50.9	1.72	13.8	12.40	6.68	11.27	2.33	0.14	0.17	99.6	0.116	49.0	0.296	38D-2
39D-a	T	51.0	1.72	13.8	12.49	6.57	11.23	2.40	0.15	0.16	99.7	0.122	48.4		
39D-b	T	50.9	1.44	14.4	11.02	7.37	12.17	2.29	0.16	0.13	100.1	0.153	54.4		
40D	T	50.3	0.99	15.3	9.49	8.67	13.26	1.96	0.07	0.08	100.3	0.096	62.0		
41D-a	T	50.7	1.33	14.5	11.19	7.56	12.00	2.26	0.11	0.12	100.0	0.113	54.6		
41D-b	T	50.7	1.24	14.6	10.98	7.69	12.18	2.23	0.11	0.11	100.0	0.119	55.5	0.198	41D-7
41D-c	T	50.8	1.38	14.2	11.49	7.27	11.87	2.26	0.12	0.13	99.8	0.124	53.0	0.219	41D-1
42D-a	N	50.8	0.77	14.9	9.28	8.90	13.59	1.67	0.05	0.06	100.2	0.083	63.1		
42D-b	T	50.7	0.86	14.9	9.57	8.78	13.30	1.73	0.06	0.07	100.1	0.098	62.1		
43D	N	50.4	0.89	14.9	9.27	8.70	13.51	1.90	0.04	0.05	99.8	0.068	62.6	0.101	43D-1
44D	T	49.5	1.10	15.5	9.91	8.58	12.52	2.10	0.08	0.07	99.5	0.098	60.7		
45D	T2	50.2	1.26	15.0	10.35	8.03	11.97	2.27	0.09	0.08	99.4	0.099	58.0	0.200	45D-2
46D	T	50.8	1.24	14.5	10.39	7.84	12.40	2.18	0.11	0.08	99.7	0.119	57.4		
47D	T	50.6	1.66	13.9	12.11	6.71	11.23	2.50	0.16	0.13	99.2	0.131	49.7		
48D-a	N	50.3	1.18	14.8	10.31	8.05	12.50	2.24	0.07	0.07	99.7	0.081	58.2		
48D-b	T	50.6	1.66	13.9	12.10	6.72	11.23	2.53	0.16	0.13	99.3	0.137	49.7	0.299	48D-4
49D	T	50.7	1.73	13.6	12.69	6.58	10.85	2.57	0.15	0.12	99.2	0.120	48.0	0.308	49D-1
50D	T	50.6	1.32	14.5	10.49	7.80	12.18	2.24	0.14	0.10	99.6	0.142	57.0	0.216	50D-1

Table 2. Major element and H_2O data[a]

Group[b]	MORB-Type[c]	SiO_2	TiO_2	Al_2O_3	FeO	MgO	CaO	Na_2O	K_2O	P_2O_5	Total	K/Ti	Mg#[d]	H_2O	Sample number[e]
51D	T	50.7	1.30	14.4	10.65	7.70	12.47	2.34	0.09	0.07	99.9	0.093	56.3		
52D	T	50.7	1.63	14.0	11.96	6.94	11.26	2.58	0.14	0.12	99.5	0.121	50.9		
53D	T	50.9	1.94	13.3	13.35	6.10	10.61	2.55	0.15	0.14	99.2	0.105	44.9		
54C	T2	50.2	1.21	15.4	9.70	8.40	12.38	2.09	0.11	0.07	99.7	0.127	60.7		
55D-a	T	50.7	1.56	14.1	11.58	7.19	11.49	2.30	0.15	0.13	99.4	0.133	52.5		
55D-b	T2	50.7	1.75	13.8	12.26	6.76	10.99	2.43	0.18	0.15	99.2	0.143	49.6		
55D-c	T2	50.7	1.82	13.7	12.50	6.65	10.86	2.38	0.19	0.15	99.1	0.144	48.7		
56D	T	50.5	1.42	14.4	11.26	7.42	11.79	2.31	0.11	0.10	99.5	0.105	54.0	0.227	56D-2
57D	T2	50.8	1.78	13.7	12.32	6.54	10.98	2.45	0.19	0.15	99.1	0.149	48.6		
58D	T	50.5	1.56	14.0	12.05	7.03	11.37	2.40	0.12	0.10	99.3	0.106	51.0	0.252	58D-2
59D	T	51.2	1.273	14.40	10.50	7.552	12.03	2.22	0.10	0.10	99.6	0.105	56.2		
60D	T	50.5	1.34	14.6	10.88	7.74	12.14	2.15	0.09	0.12	99.7	0.095	55.9		
61D	T	51.0	1.29	14.5	10.51	7.64	12.31	2.21	0.10	0.11	99.8	0.111	56.4		
62D	T3	49.2	1.28	15.4	10.81	7.97	11.72	2.40	0.09	0.11	99.1	0.093	56.8	0.215	62D-1
63D-a	N	50.4	1.31	14.4	10.62	7.79	12.21	2.15	0.06	0.10	99.3	0.068	56.6	0.172	63D-1
63D-b	T3	49.3	1.28	15.4	10.87	7.99	11.72	2.40	0.09	0.12	99.3	0.099	56.7	0.211	63D-2
64D	T	50.6	1.55	14.3	10.98	7.13	11.71	2.44	0.13	0.16	99.2	0.118	53.6		
65D	T	51.0	1.32	14.3	10.95	7.52	12.12	2.05	0.10	0.11	99.7	0.102	55.1		
66D	N	50.6	1.23	15.1	10.24	8.31	12.15	2.08	0.08	0.10	100.1	0.086	59.1		
67D	T2	50.1	1.41	15.1	10.61	8.01	11.80	2.25	0.11	0.13	99.7	0.111	57.3	0.265	67D-1
68D-a	T2	50.4	1.68	14.3	11.61	7.54	11.22	2.25	0.14	0.17	99.6	0.114	53.7		
68D-b	T2	50.4	1.68	14.2	11.56	7.79	11.10	2.23	0.14	0.16	99.4	0.114	54.6		
69D	T2	50.4	1.65	14.1	11.77	7.72	11.11	2.28	0.13	0.16	99.6	0.107	53.9	0.288	69D-1
70D	T2	50.6	1.58	14.5	11.22	7.72	11.49	2.24	0.11	0.15	99.8	0.093	55.1	0.259	70D-1
71D-a	N	49.5	1.00	16.3	9.03	9.52	12.47	2.16	0.04	0.07	100.3	0.058	65.3	0.153	71D-1
71D-b	N	49.7	1.02	16.5	9.04	9.12	12.65	2.17	0.04	0.08	100.4	0.050	64.2		
72C	N	50.6	1.20	15.5	9.43	8.58	12.36	2.15	0.07	0.09	100.1	0.082	61.9		
73D	T	48.8	0.92	17.1	9.31	9.29	12.32	2.27	0.07	0.06	100.3	0.108	64.0	0.144	73D-1
74D	N	50.2	1.10	15.5	9.18	8.56	12.71	2.23	0.05	0.08	99.8	0.068	62.4		
75D	N	51.1	1.42	14.4	11.09	7.26	11.66	2.56	0.08	0.11	99.9	0.079	53.8		
76D	N	50.9	1.10	15.1	9.46	8.34	12.71	2.06	0.06	0.09	100.0	0.077	61.1	0.221	75D-1
77D-a	N	50.6	1.22	15.1	9.81	8.20	12.60	2.23	0.05	0.10	100.1	0.062	59.9	0.157	77D-2
77D-b	N	50.8	1.27	14.9	10.03	7.97	12.43	2.28	0.05	0.10	100.0	0.059	58.6		
78D-scor	E2	48.7	3.06	14.2	11.73	6.15	11.34	2.99	0.55	0.36	99.2	0.249	48.3	0.181	78D-1
79D	N	49.0	1.01	16.7	9.73	8.87	12.05	2.48	0.04	0.07	100.2	0.059	61.9	0.160	79D-1
80D	N	49.9	1.13	15.8	9.15	8.70	12.59	2.51	0.03	0.08	100.0	0.040	62.9	0.109	80D-2
81D	N	48.8	0.90	17.0	8.24	9.55	12.67	2.33	0.03	0.05	99.8	0.045	67.4		
82D	N	48.1	1.01	17.5	8.88	9.28	12.15	2.48	0.02	0.06	99.6	0.031	65.1		
83D	N	49.9	1.23	15.6	9.51	8.60	11.99	2.23	0.05	0.09	99.3	0.051	61.7		
84D	N	50.3	1.30	14.60	9.82	7.95	12.28	2.19	0.06	0.11	98.7	0.061	59.1	0.154	84D-4
85D	N	50.5	1.34	14.5	9.77	7.88	12.33	2.35	0.05	0.10	99.0	0.054	59.0		
86D-a	N	50.1	1.25	14.7	9.63	8.17	12.34	2.09	0.06	0.10	98.6	0.064	60.2		
86D-b	N	49.9	1.35	14.9	9.85	8.27	12.19	2.10	0.06	0.11	98.9	0.064	59.9		
87D	N	50.4	1.18	15.1	9.30	8.35	12.65	2.24	0.05	0.09	99.5	0.055	61.6		
88D	N	50.5	1.16	15.1	9.20	8.56	12.61	2.08	0.05	0.08	99.5	0.060	62.4	0.130	88D-1
89D	N	50.7	1.31	14.8	9.66	8.13	12.39	2.13	0.06	0.10	99.4	0.059	60.0		
90C-a	N	50.9	1.68	14.00	11.84	6.82	11.44	2.21	0.08	0.14	99.3	0.067	50.7		
90C-b	N	50.6	1.59	14.2	10.73	7.46	11.85	2.38	0.07	0.12	99.1	0.059	55.3		
91D	N	50.0	1.09	15.5	9.11	8.95	12.50	2.06	0.04	0.08	99.5	0.057	63.7		
92D	N	50.0	1.39	15.0	9.76	8.46	11.87	2.25	0.07	0.12	99.1	0.071	60.7	0.186	92D-1
1538_PR	T	50.7	1.76	14.05	11.94	6.99	11.23	2.34	0.13	0.16	99.5	0.102	51.1		
1539-a_PR	T	50.6	1.70	14.17	11.93	7.21	11.34	2.37	0.12	0.14	99.8	0.102	51.9		
1539-b_PR	T	51.0	1.84	13.63	12.54	6.57	11.28	2.35	0.14	0.17	99.8	0.104	48.3		
1540-a_PR	T	51.0	1.92	13.37	13.12	6.29	10.96	2.40	0.15	0.16	99.6	0.109	46.1		
1540-b_PR	T	51.0	1.59	14.18	11.84	7.25	11.40	2.32	0.12	0.13	100.0	0.104	52.2		
1541_PR	T	51.2	1.57	14.12	11.66	7.13	11.43	2.34	0.12	0.14	99.9	0.107	52.1		
1544_PR	N	51.1	1.69	13.93	11.81	7.05	11.74	2.29	0.11	0.15	100.0	0.090	51.6		
1545-a_PR	T	50.6	1.78	14.11	11.91	7.18	11.17	2.30	0.13	0.16	99.5	0.103	51.8		
1545-b_PR	N	50.3	1.05	15.41	9.62	8.79	12.68	1.88	0.05	0.08	100.0	0.070	62.0		
1549-a_PR	T2	50.8	1.67	14.13	11.94	7.45	11.22	2.31	0.13	0.15	100.0	0.108	52.7		
1549-b_PR	N	50.6	0.99	15.50	9.62	8.86	12.96	1.87	0.05	0.07	100.7	0.072	62.1		
1551-a_NG	N	49.9	1.11	16.19	9.35	8.60	12.56	2.46	0.05	0.09	100.4	0.066	62.1		

Table 2. Major element and H_2O data[a]

Group[b]	MORB-Type[c]	SiO_2	TiO_2	Al_2O_3	FeO	MgO	CaO	Na_2O	K_2O	P_2O_5	Total	K/Ti	Mg#[d]	H_2O	Sample number[e]
1551-b_NG	T	50.4	1.14	15.58	9.73	9.00	11.79	2.31	0.08	0.09	100.3	0.096	62.3		
1554-a_NG	N	49.9	1.12	16.33	9.46	8.77	12.36	2.36	0.05	0.08	100.6	0.062	62.3		
1554-b_NG	N	50.4	1.29	15.77	10.00	8.39	12.01	2.38	0.06	0.09	100.6	0.061	59.9		
1554-c_NG	N	50.3	0.95	16.14	8.60	9.13	13.06	2.16	0.05	0.06	100.6	0.071	65.4		
1554-d_NG	N	49.6	1.04	16.45	9.15	9.67	12.20	2.25	0.04	0.07	100.6	0.053	65.3		
1555_DR	N	51.1	1.14	15.13	9.59	8.48	12.60	2.11	0.06	0.08	100.5	0.073	61.2		
1557-a_PR	T	50.8	1.88	13.34	13.28	6.31	10.88	2.39	0.15	0.16	99.4	0.111	45.9		
1557-b_PR	T	50.8	1.66	13.80	12.42	6.85	11.30	2.34	0.13	0.15	99.7	0.106	49.6		
1557-c_PR	T	51.0	1.55	14.18	11.85	7.23	11.38	2.33	0.12	0.14	99.9	0.105	52.1		
A6_PR	T2	50.6	1.71	13.98	11.98	7.47	11.04	2.32	0.13	0.15	99.5	0.104	52.6		
A13_DR	N	51.1	1.25	14.61	10.08	7.97	12.36	2.13	0.08	0.10	99.9	0.084	58.5		
Precision[f]		0.1	0.015	0.05	0.06	0.07	0.05	0.03	0.004	0.006					

[a]Oxide values listed in wight percent. Compositions for major elements are averages of analyses for all individual samples within a group.

[b]Sample group names are the station number followed by the sampling method: D-dredge or C-wax core. Alvin and Atlantis samples are named according to the dive number or dredge number (preceded by "A"), respectively, and the segment: PR-propagating rift (2°40'N), NG-North Graben (2°25'N), or DR-Dying Rift (2°19'N). In cases of more than one group per station, groups are distinguished as a, b, or c.

[c]See text for explanation of MORB-type classification.

[d]Mg# is calculated by molar MgO/(MgO + FeO*).

[e]Number of the individual sample on which H_2O analysis was performed; sample was chosen to represent the group.

[f]Precision for the major element analyses was estimated from standard deviations of groups represented by a large number of individual samples (9 or more).

Table 3. Empirical slopes calculated for $MgO_{(8.0)}$ adjustments

	N		T[a]		E[a]	
Oxide	slope	samples included[b]	slope	samples included[b]	slope	samples included[b]
			Best fit line.[c] y = mx + b			
SiO_2	-0.31	< 8.5% MgO	-0.31	< 8.5% MgO	-0.27	> 4.0 wt.% MgO
Al_2O_3	0.79	< 8.5% MgO	0.79	< 8.5% MgO	0.68	> 4.0 wt.% MgO
FeO*	-1.28	< 8.5% MgO	-1.28	< 8.5% MgO	-1.28	> 4.0 wt.% MgO
CaO	0.55	< 8.5% MgO	0.55	< 8.5% MgO	1.13	All
			Treated as incompatible elements[d]; fitted with power law curves: $y = a*x^m$			
TiO_2	-1.59	< 8.5% MgO	-1.59	< 8.5% MgO	-1.28	> 4.0 wt.% MgO
Na_2O	-0.51	< 8.5% MgO	-0.51	< 8.5% MgO	-0.34	All
K_2O	-1.41	< 8.5% MgO	-1.99	< 8.5% MgO	-1.61	All
P_2O_5	-1.89	< 8.5% MgO	-1.89	< 8.5% MgO	-1.66	All
H_2O	-2.70	< 8.5% MgO	-2.70	< 8.5% MgO	-1.57	All

[a]No T2, T3, or E2 samples were used to calculate slopes of lines or curves, with the exception of H_2O, for which T2 and T3 data were included for curve fitting. However, all E2, T2, and T3 data were corrected using the equations and slopes as used for the "regular" groups (i.e., T1 and E1).

[b]In most cases, samples with MgO contents < 3.5 wt% or >8.5 wt % were excluded. Exceptions arose only when the trend of the data was not affected by the appearance of a new phase at these breaks.

[c]For SiO_2, Al_2O_3, FeO*, and CaO, a line with the equation $y = mx + b$ was fit to the data.

[d]Incompatible elements TiO_2, Na_2O, K_2O, P_2O_5, and H_2O were modeled using the equation for a power law curve: $y = a*x^m$.

Table 4. Model input values

	Region Represented	K	H_2O	Na_2O	Ti	Z_{cr}[a]
N-MORB	West of 95.5°W	500[b]	1600	2.15	7200	5.7
T-MORB	95.5°W to 92.7°W	750	1600	2.15	7200	6.3
E-MORB	East of 92.7°W	1575	2800	2.45	9900	7.5
uncertainty		83	290	0.12	540	
Bulk distribution coefficient (*D*)		0.0024[c]	0.01[d]	0.03[e]	0.08[f]	

[b]Crustal thickness, in km.

[a]Average fractionation-adjusted values for all samples within a MORB-type. K, H_2O, and Ti values are listed as parts per million (ppm); Na_2O values are listed as oxide weight percent.

[c]*Niu et al.* [1996]

[d]*Dixon et al.* [1988]; *Michael* [1995]

[e]*Langmuir et al.* [1992]

[f]*Johnson et al.* [1990]; *Niu et al.* [1996]

Table 5. Variables used in model

	Variable	Description	Known from	Range Allowed	Step Size
input	Z_{cr}	observed crustal thickness, in km	reflection/refraction experiments done during the G' expedition [*Canales et al*, 2002]		
input	$C_L^{\ i}{}_{obs}$	concentration of an element (i) in glass, average for all samples of same MORB-type	backtracking of geochemical data to parental magma composition at 8.0 wt.% MgO		
input	D	bulk distribution coefficients	published estimates [e.g., *Dixon et al.*, 1988; *Johnson et al*, 1990; *Langmuir et al.*, 1992; *Michael*, 1995; *Niu et al.*, 1996]		
variable	$C_0^{\ Na}$	initial concentration of Na in source	variable	N-MORBs: 1500-2600 ppm T-MORBs: 1000-2600 ppm E-MORBs: 1000-3000 ppm	100 ppm 100 ppm 100 ppm
variable	U_w/U_0	flow rate of material in hydrous region, relative to flow (spreading) rate in anhydrous melting region	variable	N-MORBs: 1-2 T-MORBs: 1-10 E-MORBs: 1-10	0.2 0.5 0.5
variable	h_w	depth from anhydrous solidus to volatile-present solidus, in km	variable	N-MORBs: 0-46 km T-MORBs: 0-50 km E-MORBs: 0-74 km	2 km 2 km 2 km
variable	h_D	depth to dry solidus, in km	variable	1-100 km	0.5 km
variable	B_w	productivity in wet melting region, melt fraction per km	based on estimates of averages in low-productivity melting regions [*Asimow et al.*, 2001]	0.0003 to 0.0005 /km	0.0001 /km
output/ constraint	B_D	productivity in dry melting region, melt fraction per km f(Z_{cr}, U_w/U_0, B_w, h_w)	estimates of averages in high-productivity region of melting (*Asimow et al.*, 2001)	0.0027 – 0.0053 /km (0.8 - 1.6 %/kbar)	
output/ constraint	$h_w/C_0^{\ H2O}$	relationship between water content in mantle and the depression of the solidus	activity of H_2O in olivine [*Hirth and Kohlstedt*, 1996] plus revision due to calibration errors [*Bell et al.*, 2003]. See text for discussion.	between 0.24 and 0.26 km/ppm	
output	$C_L^{\ i}{}_{pred}$	predicted concentation of element in parental magma	hydrous melting equation (see text)		
output	$C_0^{\ i}$	initial concentration of element in source (i = K, H_2O, Ti)	calculated relative to C_0^{Na} and $C_{L\,obs}^{\ i}$		
output	$\overline{F}$	mean fraction of melting over entire melting region	hydrous melting equation (see text)		
output	F_{max}	maximum degree of melting in entire melting region	f (U_w,h_w,F_w,Z_{cr},h_D)		
output	F_w	degree of melting in additional zone of hydrous melting	B_w*h_w		

Table 6. Range of model inputs that can combine to match G' data[a]

	MORB type	C_0^K (ppm)	C_0^{H2O} (ppm)	C_0^{Na2O} (ppm)	C_0^{Ti} (ppm)	B_w %/km	h_w km	F_w fraction	B_D %/km	h_D km	$\overline{F}$ fraction	F_{max} fraction	U_w/U_0
Dry1[b]		41	136	2100	991	0	0	0	0.2643	60.5	0.080	0.160	1
Dry2		53	175	2600	1136	0	0	0	0.4473	46.5	0.104	0.208	1
min[c]	**N**	26	107	1900	955	0.04	26	0.010	0.2746	54.0	0.046	0.159	2
max		35	141	2400	1113	0.03	36	0.011	0.4870	41.5	0.062	0.213	1
midpoint[d]		32	124	2100	1012	0.04	32	0.013	0.3336	49.0	0.060	0.176	1
Dry1		65	144	2200	1020	0	0	0	0.2694	63.0	0.085	0.170	1
Dry2	**T**	86	190	2800	1197	0	0	0	0.4840	47.0	0.114	0.227	1
min		21	77	1700	934	0.04	20	0.008	0.3387	49.5	0.021	0.176	10
max		56	146	2500	1148	0.04	36	0.014	0.5081	42.0	0.069	0.228	1
Dry1		148	275	2700	1469	0	0	0	0.2712	68.5	0.093	0.186	1
Dry2	**E**	168	309	3000	1572	0	0	0	0.3477	60.5	0.105	0.210	1
min		37	110	1700	1211	0.04	28	0.011	0.3181	51.5	0.019	0.175	10
max		105	237	2800	1591	0.03	58	0.017	0.5013	45.0	0.062	0.243	1

[a]Solutions listed produce magma compositions that match G' crustal thickness and composition values listed in Table 4. These maximum and minimum values, normalized to the N-MORB midpoint value, were used to plot Figure 9. Symbols are explained in Table 5 and text.

[b]Dry solutions are the minimum (Dry1) and maximum (Dry2) of all solutions predicted by the anhydrous pooled melting equation [3] that fit our inputs and constraints. All variables that were used to create these minimum and maximum solutions are listed, as well as corresponding model outputs. By definition, anhydrous solutions have F_w, B_w, and $h_w = 0$.

[c]Minimum (min) and maximum (max) source concentrations predicted by the hydrous melting equation [11].

[d]Midpoint source concentration values are used as normalizing values for all other solutions when plotting Figure 9. The input variables that created this solutions are closest to the midpoint of the range allowed for each input variable, with the exception of U_w/U_0, for which only passive upwelling (U_w/U_0=1) was allowed.

Figure Captions

Figure 1. Location of Galápagos Spreading Center (GSC) relative to Central and South America, the East Pacific Rise (EPR), and the Galápagos Archipelago. The east-west trending GSC separates the Cocos and Nazca plates. Study area detailed in Figure 2 is outlined in black.

Figure 2. Bathymetric map of study area with sampling stations. High-resolution bathymetry collected during G' cruise is superimposed on satellite-derived E-TOPO5 bathymetry. Numbers represent dredge (circles) and wax core (diamonds) sampling stations. Stars indicate locations of Hey et al. (1992) samples used in this study. The ridge axis is shown with a thin white line. Note transition from axial valley morphology in the west, to axial high morphology in the east.

Figure 3. K/Ti atomic ratios versus MgO show the classification into N-, T- and E-MORB types. N-MORBs, with K/Ti < 0.09, are represented by purple diamonds; T-MORBs, with K/Ti between 0.09 and ~0.15, are red circles; and E-MORBs, with K/Ti >0.15 and K_2O >0.20, are shown by light blue triangles.

Figure 4. Major element oxides plotted versus MgO. Rocks evolved from the same parental magma are expected to fall on single liquid lines of descent. Variation among MORB types (see discussion of classification in text) is illustrated here.

Figure 5. H_2O versus MgO (**a**) and K_2O (**b**). Symbols as in Figure 4. The incompatible nature of H_2O is evident from the positive correlation with K_2O; the slope indicates that the bulk distribution coefficient (D) for K_2O is less than D_{H2O}.

Figure 6. Along-axis compositional variations. Bathymetric map (**a**) is included at the same longitudinal scale to show ridge features that correspond with compositions. (**b**)-(**e**) and (**g**)-(**i**) are fractionation-adjusted compositions. Gray shaded boxes delineate the three major provinces, defined by correlated geochemical, geophysical, and bathymetric characterisitcs [Detrick et al., 2002]. Open symbols in (**f**) indicate samples with anomalously high K/Ti ratios created by fractionation of Ti-bearing oxides, not elevated K_2O contents.

Figure 7. Residual Melting Column (RMC) as illustrated by Plank and Langmuir [1992] (a) and modified to include an additional zone of hydrous melting that is created by the depression of the solidus when water is present in the mantle (b). Illustrations are not drawn at the same scale. The RMC is the net residue of melting. Black arrows indicate solid mantle flow. Dashed contour lines indicate extent of melting in the melting region (triangular area) and extent of melt depletion in the RMC. (**a**) In an anhydrous melting region, contours are evenly spaced because productivity is assumed to be constant. h is the depth to the solidus. The width of the RMC, U, is controlled by the flow rate of mantle material, which is assumed to be constant and equal to the spreading rate of the ridge. In this case, $\overline{F}$ is ½ F_{max}, enrichment of an element in the melt can be calculated from equation [3], and crustal thickness is simply the RMC area multiplied by $\overline{F}$. (**b**)

RMC concept modified to include an additional zone of hydrous melting (purple area). We have relaxed the assumption of passive upwelling and constant melt productivity. Flow rate through the hydrous region (U_w) may be the same as, or higher than, flow rate through the anhydrous region (U_0), as indicated by the greater thickness of the arrows. Productivity in the hydrous region (B_w) is probably lower than productivity in the anhydrous region (B_D) (see text). Depth to the dry solidus is now denoted as h_D; additional depth to the hydrous solidus is h_w; the total depth of melting is $h_D + h_w$. Mean melt fraction ($\overline{F}$) and melt composition (equations [12] and [11], respectively) now take into account contributions from both the hydrous and anhydrous melting regions.

Figure 8. General solutions to the hydrous melting equation. (**a**) Effects of variable upwelling rates on mean degree of melting using the hydrous melting equation (curves), compared to the $\overline{F}$ solution using the anhydrous pooled melting equation (blue dot). All calculations are for a melting region with constant depth to the dry solidus (h_D=50 km) and constant melt productivity in the dry region (B_D=0.36 %/km). Hydrous solutions use B_w =0.045 %/km. Various upwelling rates were modeled, fromU_w/U_0=1-5 (U_w/U_0=4 not shown); higher upwelling rates produce lower $\overline{F}$ values at a given h_w. (**b**) Effects of h_w, U_w/U_0, and B_w on incompatible element enrichment (relative to the source) at various degrees of melting. Solid black line is C_l/C_0 predicted by the pooled melting equation of Plank and Langmuir [1992] for an element with D=0.01; all other lines are predictions based on the hydrous melting equation. All predictions are for an element with D=0.01. Red solid line can be considered a "standard" model, with mid-range values of h_w, B_w, and U_w/U_0: 30km, 0.04 %/km, and 1, respectively. All other lines have the same values

for two of the variables, and the third variable has been changed. Navy: h_w=10 km; purple: h_w=50 km; red dotted: B_w=0.03 %/km; light blue: U_w/U_0=2; green: U_w/U_0=5.

Figure 9. N-MORB mantle normalized diagram showing relative range of source enrichments required to match observed G' compositions and crustal thickness for (**a**) N-MORBs and (**b**) N-, T-, and E-MORBs. All source enrichments are measured relative to a "midpoint" N-MORB composition that was chosen because the variables h_w, B_w, and C_0^{Na} are near the median of the values for which reasonable solutions were produced. Passive upwelling, U_w/U_0 =1, is used to calculate this midpoint. See Table 6 for associated parameters. Dashed lines show the maximum enrichment required using dry melting equations for each MORB type; dotted lines show minimum source values using dry melting equations. Shaded regions show the range of values that are permitted as solutions for each MORB type when a hydrous melting component is factored in. All N-MORB solutions (hydrous or anhydrous) are shown with dark blue; T-MORB solutions are shades of red; and E-MORB solutions are shown in light blue. Hydrous melting allows *lower* source concentrations of incompatible elements to explain the G' data.

Figure 10. U_w/U_0 versus required source compositions for N-, T-, and E-MORBs. Symbols represent MORB types: N-MORB solutions are diamonds; T-MORB solutions are circles, and E-MORB solutions are triangles. Color variations within each MORB-type represent different input values for wet productivities (B_w = 0.0003, 0.0004, and 0.0005); lighter colors represent lower B_w values. C_0^{Na} values (c) are included to show the relative range of values that were allowed by the model's C_0^{H2O}/h_w and B_D constraints,

but should be regarded as allowable input variables; all other plots are outputs (results) of the model, and were calculated relative to the allowed C_0^{Na} values (see text for explanation of model). The required source concentration depends strongly on the upwelling rate. The more material that is cycled through the hydrous melting region relative to the anhydrous melting region (i.e., U_w/U_0), the less "enriched" the source is required to be.

Figure 11. Symbols as in Figure 10. (**a**) Comparison between the allowable ranges of C_0^{H2O} and $\overline{F}$ that fit observed values of crustal thickness and composition for the N-, T-, and E-MORB types. The average N-MORB solution requires lower H_2O contents in the source, and is created by higher $\overline{F}$ than the average E-MORB solution. T-MORB solutions encompass the entire range of N-MORB $\overline{F}$ solutions, but reach much lower $\overline{F}$ values than N-MORBs because T-MORB solutions were allowed to vary over a larger range of U_w/U_0 values. The positive correlation between C_0^{H2O} and $\overline{F}$ among each MORB type does not represent a universal trend; it reflects the fact that all solutions for each MORB type are matches to *one* value of Z_{cr} and C_L^{obs}. U_w/U_0 dominates the large range of both C_0^{H2O} and $\overline{F}$. (**b**) Illustration of $\overline{F}$ dependence on upwelling rate (U_w/U_0).

Figure 12. Difference between MORB types in depth to the dry solidus, h_D, plotted as a function of productivity in the anhydrous melting region, B_D. Symbols as in Figure 10. Region of solutions to N-MORB data is shaded in purple; solutions to E-MORB data are shaded light blue; area of overlap is medium blue. The B_D values we allowed as viable

solutions (0.27 – 0.53 %/km, or ~0.8-1.6%/kbar) limit the maximum and minimum h_D values. At any given B_D value, the maximum difference in h_D between N-MORBs and E-MORBs is ~9 km. This difference can be converted to a temperature difference, ΔT, using the slope of the mantle solidus (we use 3.8°C/km). The maximum ΔT between N-MORBs and E-MORBs at any given B_D value solutions is ~34°C. When similar B_w values are compared between N- and E-MORB regions, this difference reduces to as little as 3 km, or ~11°C.

Figure 13. Most likely solutions to G' data using the hydrous melting equation (filled symbols/regions), created by restricting the range of input parameters to those that are more probable (see text for discussion of parameters). Solutions created using the anhydrous pooled melting equation (open symbols) are shown for comparison. Shading in hydrous solution regions represents variation in upwelling rates. The $\overline{F}$ of N-MORB solutions (purple diamonds) is ~4% less using the hydrous melting equation than the ~10% expected from the pooled melting equation. T-MORB hydrous solutions (shaded red region) encompass the N-MORB solutions: lower $\overline{F}$ and C_0^{H2O} solutions are created by $U_w/U_0 = 1.5$; higher $\overline{F}$ and C_0^{H2O} solutions are created by passive upwelling. E-MORB solutions require a source at least somewhat enriched in H_2O relative to the source that melts to produce N- and T-MORBs. E-MORBs are also created by lower $\overline{F}$.

Figure 1

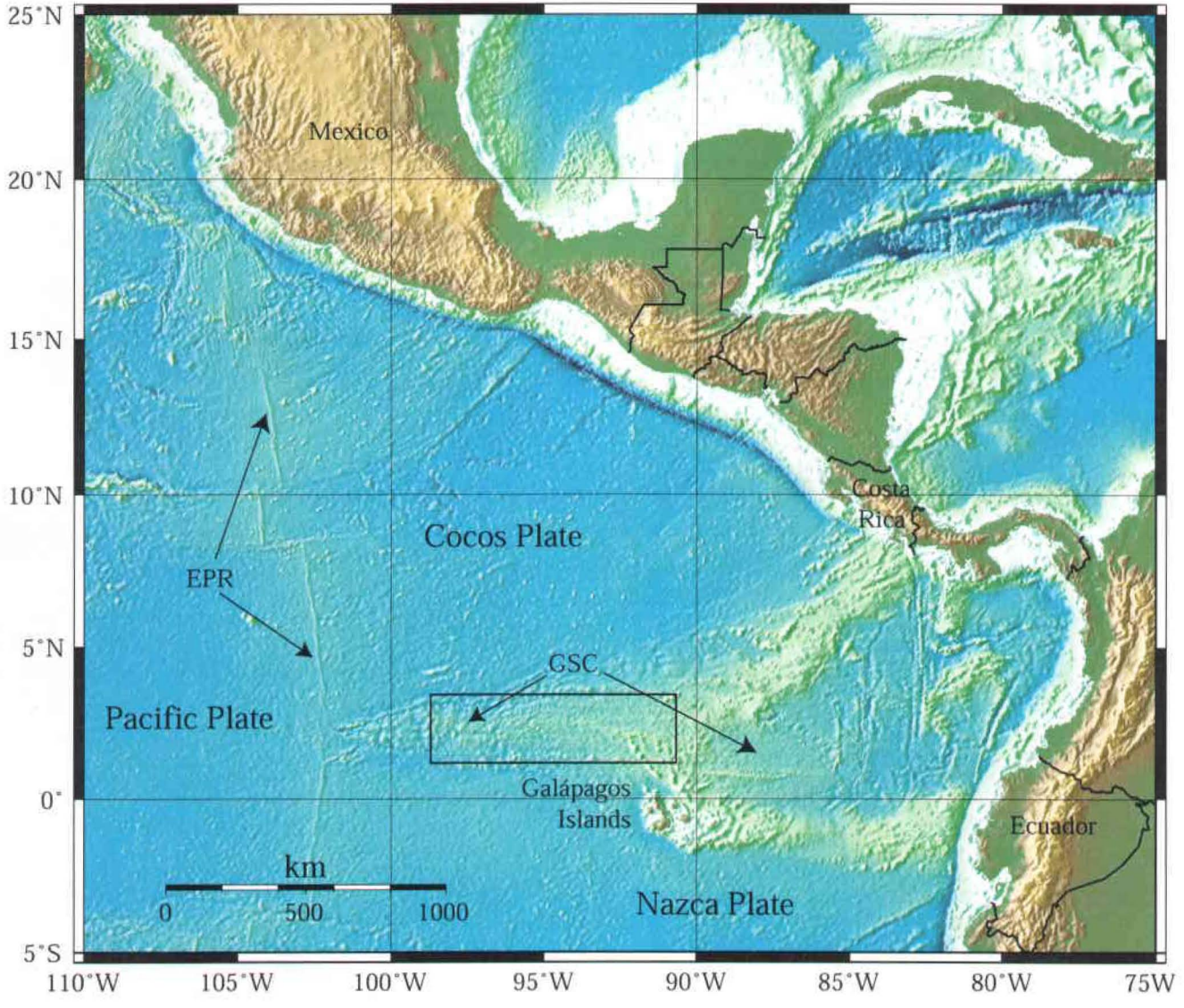
25°N
20°N
15°N
10°N
5°N
0°
5°S
110°W
105°W
100°W
95°W
90°W
85°W
80°W
75W
Mexico
Costa Rica
Cocos Plate
EPR
GSC
Pacific Plate
Galápagos Islands
Ecuador
km
0
500
1000
Nazca Plate

Figure 2

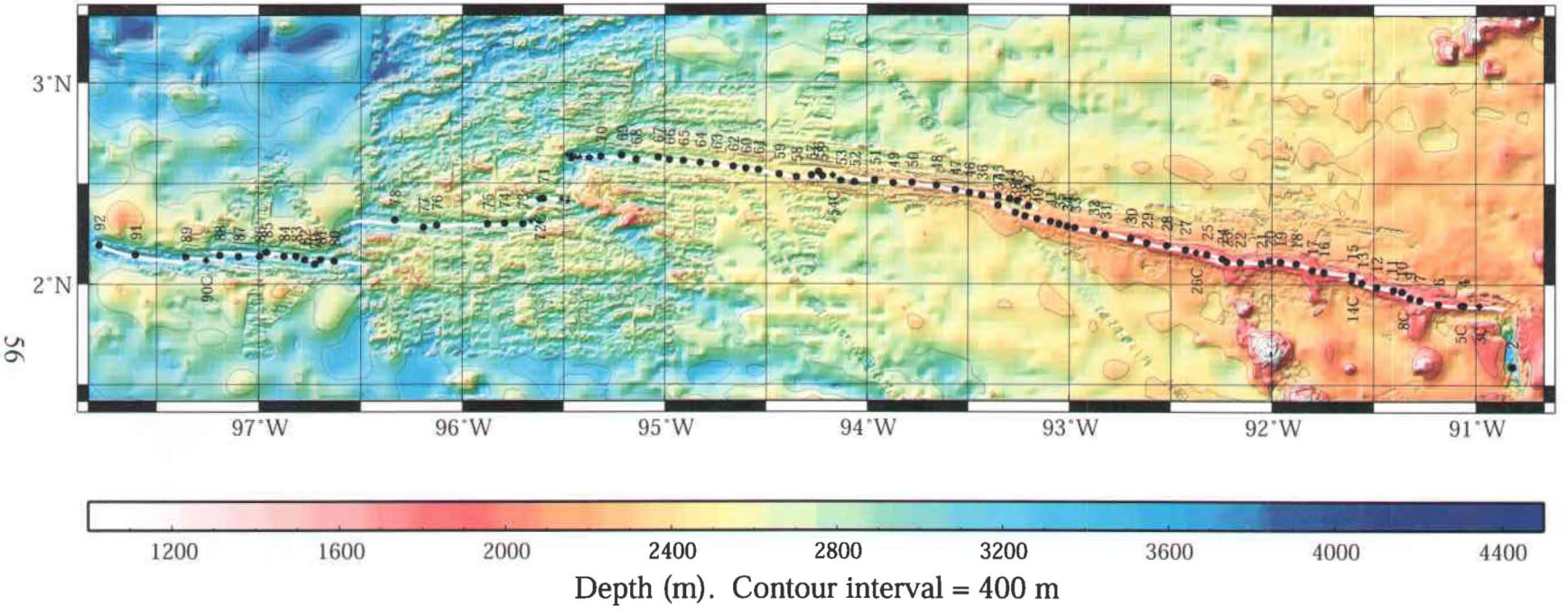
3°N
2°N
97°W
96°W
95°W
94°W
93°W
92°W
91°W
1200
1600
2000
2400
2800
3200
3600
4000
4400
Depth (m). Contour interval = 400 m

Figure 3

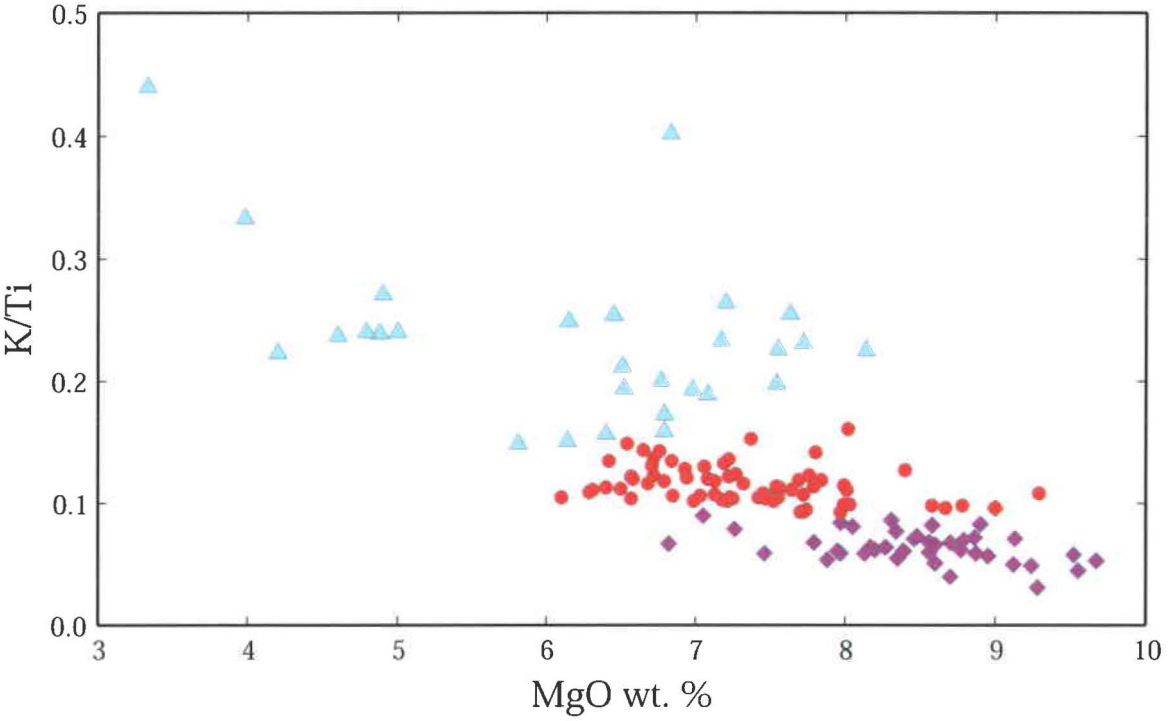

Figure 4

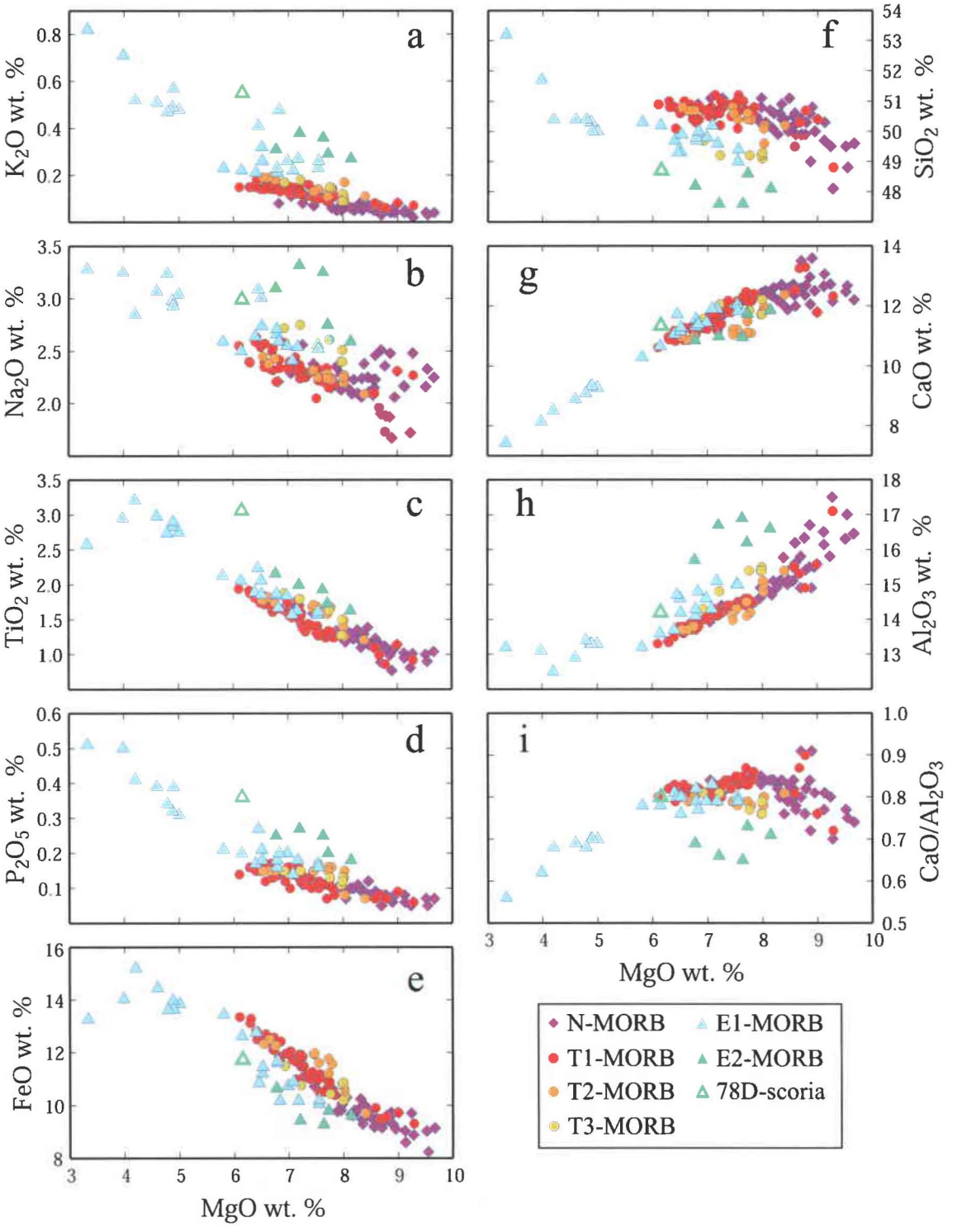
a
b
c
d
e
f
g
h
i
K_2O wt. %
Na_2O wt. %
TiO_2 wt. %
P_2O_5 wt. %
FeO wt. %
SiO_2 wt. %
CaO wt. %
Al_2O_3 wt. %
CaO/Al_2O_3
MgO wt. %
MgO wt. %
N-MORB
T1-MORB
T2-MORB
T3-MORB
E1-MORB
E2-MORB
78D-scoria

Figure 5

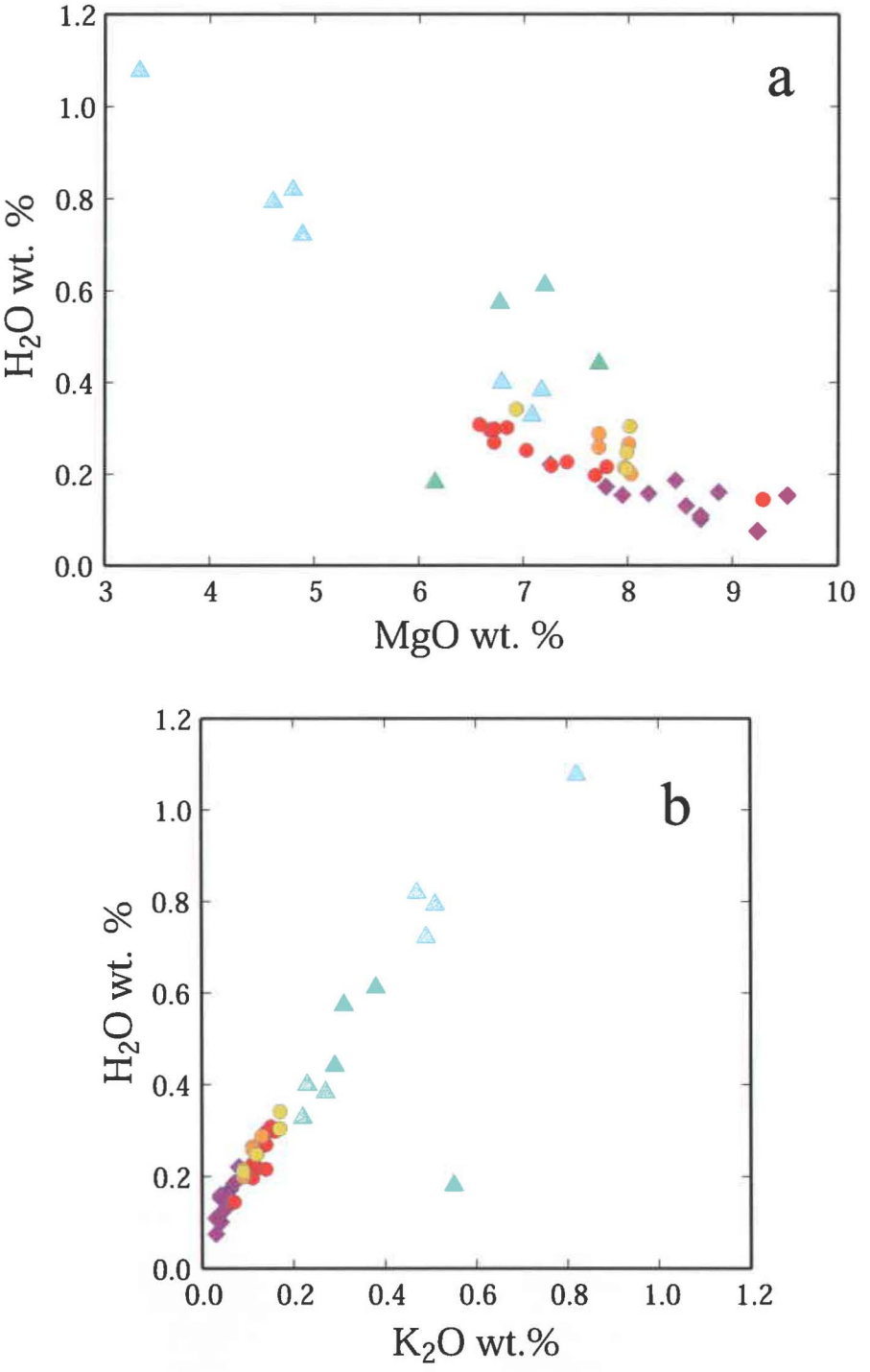
a
1.2
1.0
0.8
0.6
0.4
0.2
0.0
H2O wt. %
3
4
5
6
7
8
9
10
MgO wt. %
b
1.2
1.0
0.8
0.6
0.4
0.2
0.0
H2O wt. %
0.0
0.2
0.4
0.6
0.8
1.0
1.2
K2O wt.%

Figure 6

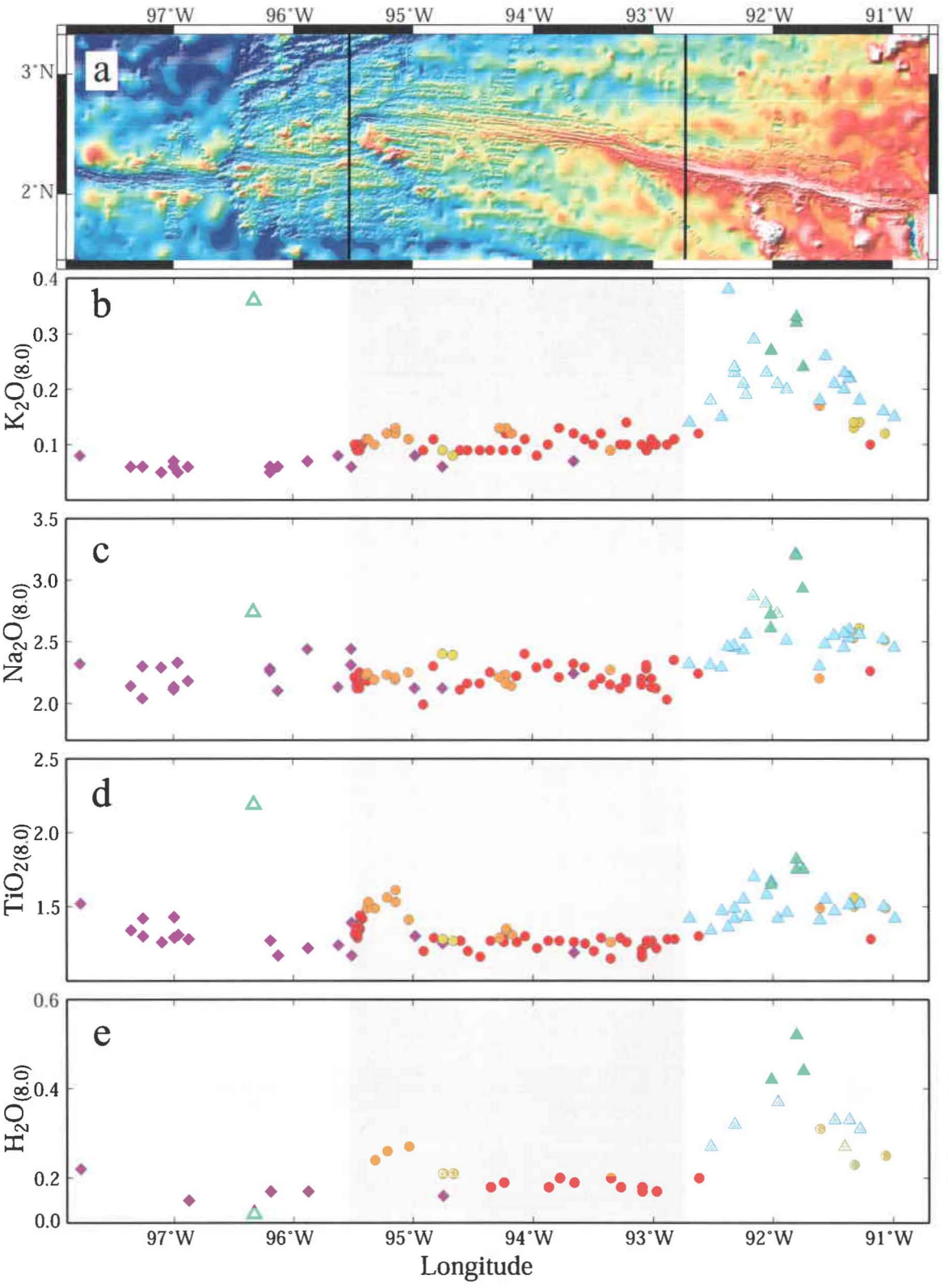
97°W
96°W
95°W
94°W
93°W
92°W
91°W
3°N
2°N
a
b
c
d
e
$K_2O_{(8.0)}$
$Na_2O_{(8.0)}$
$TiO_{2(8.0)}$
$H_2O_{(8.0)}$
Longitude

Figure 6 (cont'd)

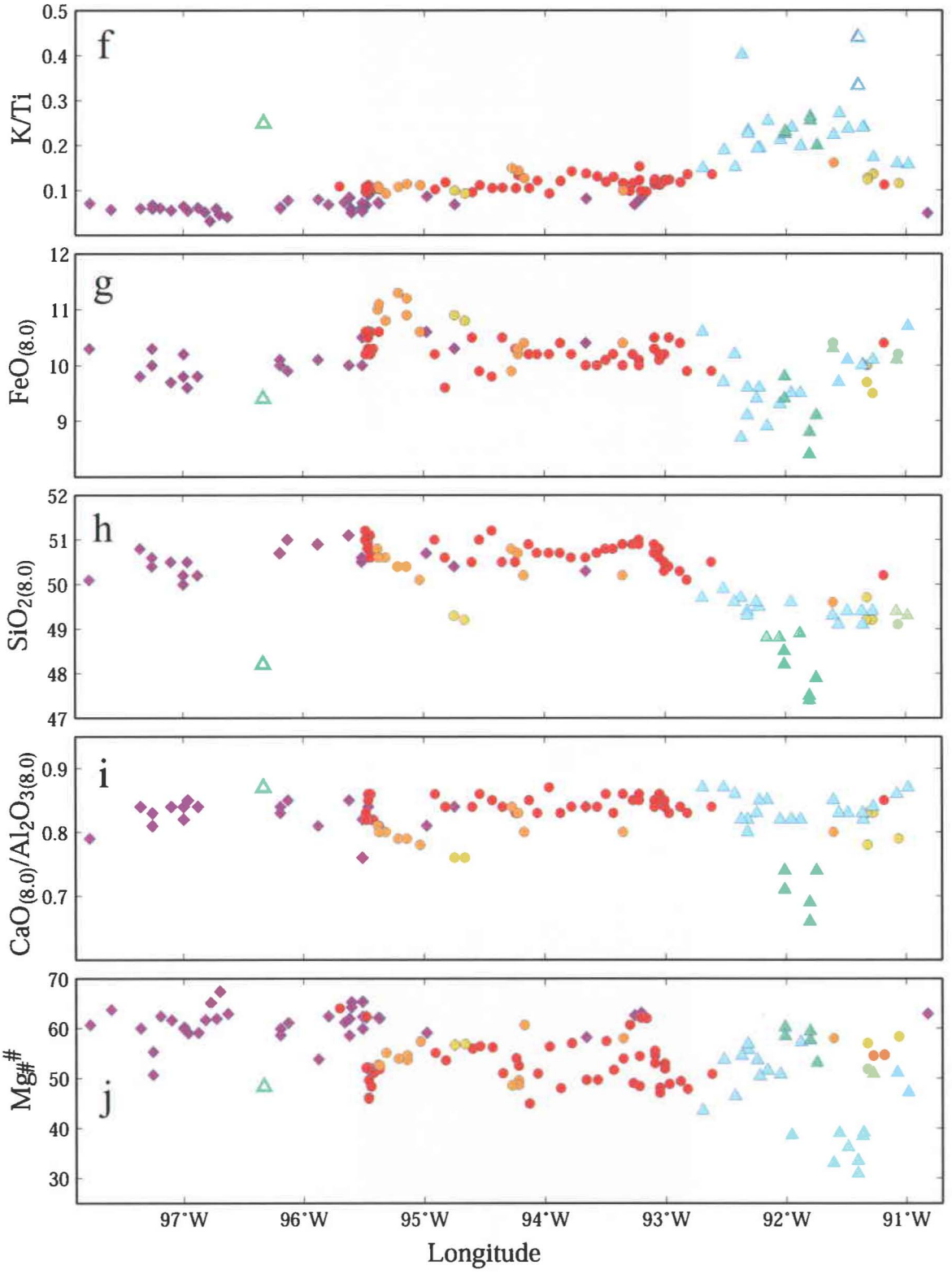

Figure 7

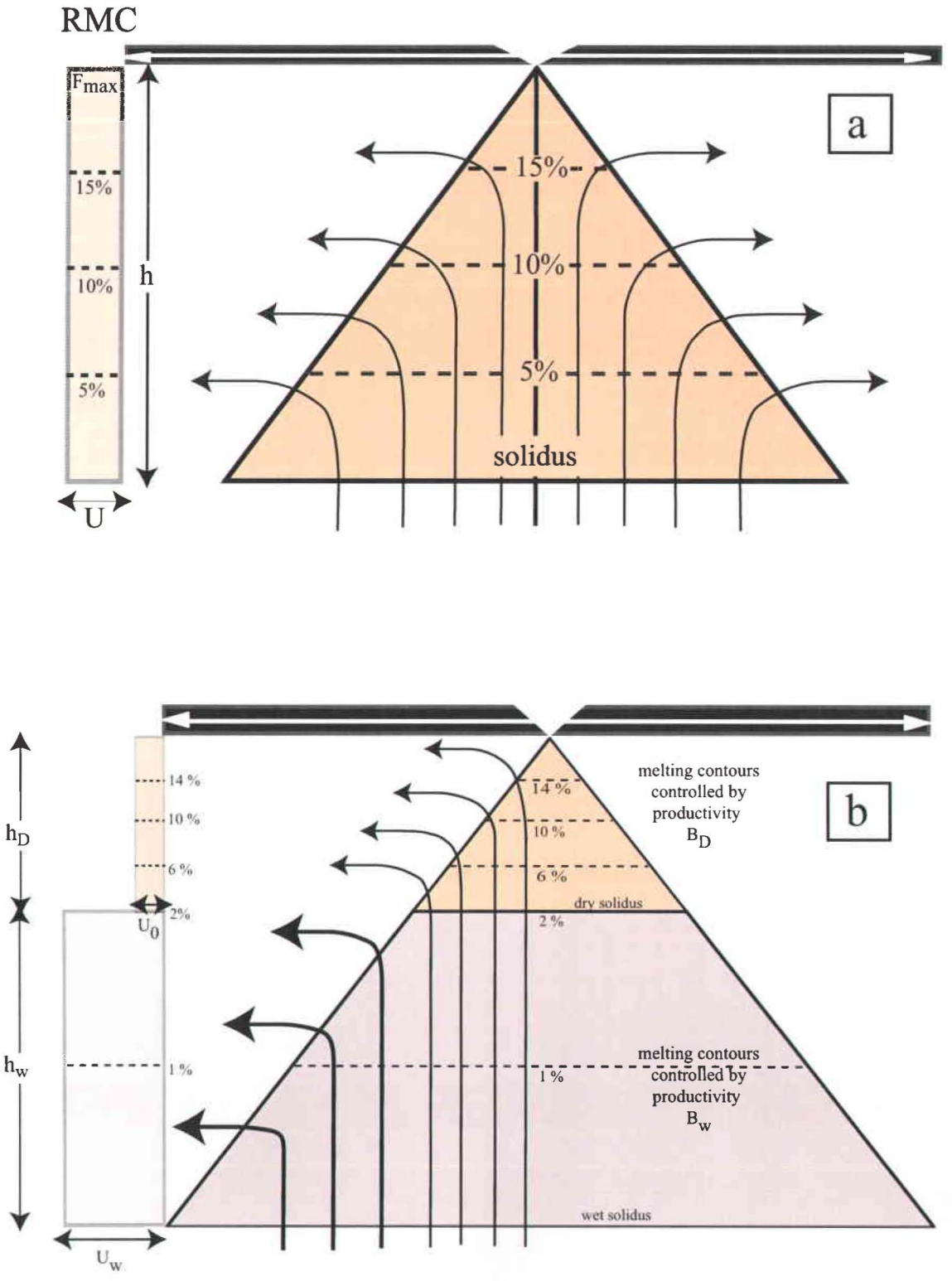
RMC
F_{max}
15%
10%
5%
h
U
a
15%
10%
5%
solidus
h_D
h_w
14 %
10 %
6 %
2%
U_0
1 %
U_w
melting contours
controlled by
productivity
B_D
b
14 %
10 %
6 %
dry solidus
2 %
melting contours
controlled by
productivity
B_w
1 %
wet solidus

Figure 8

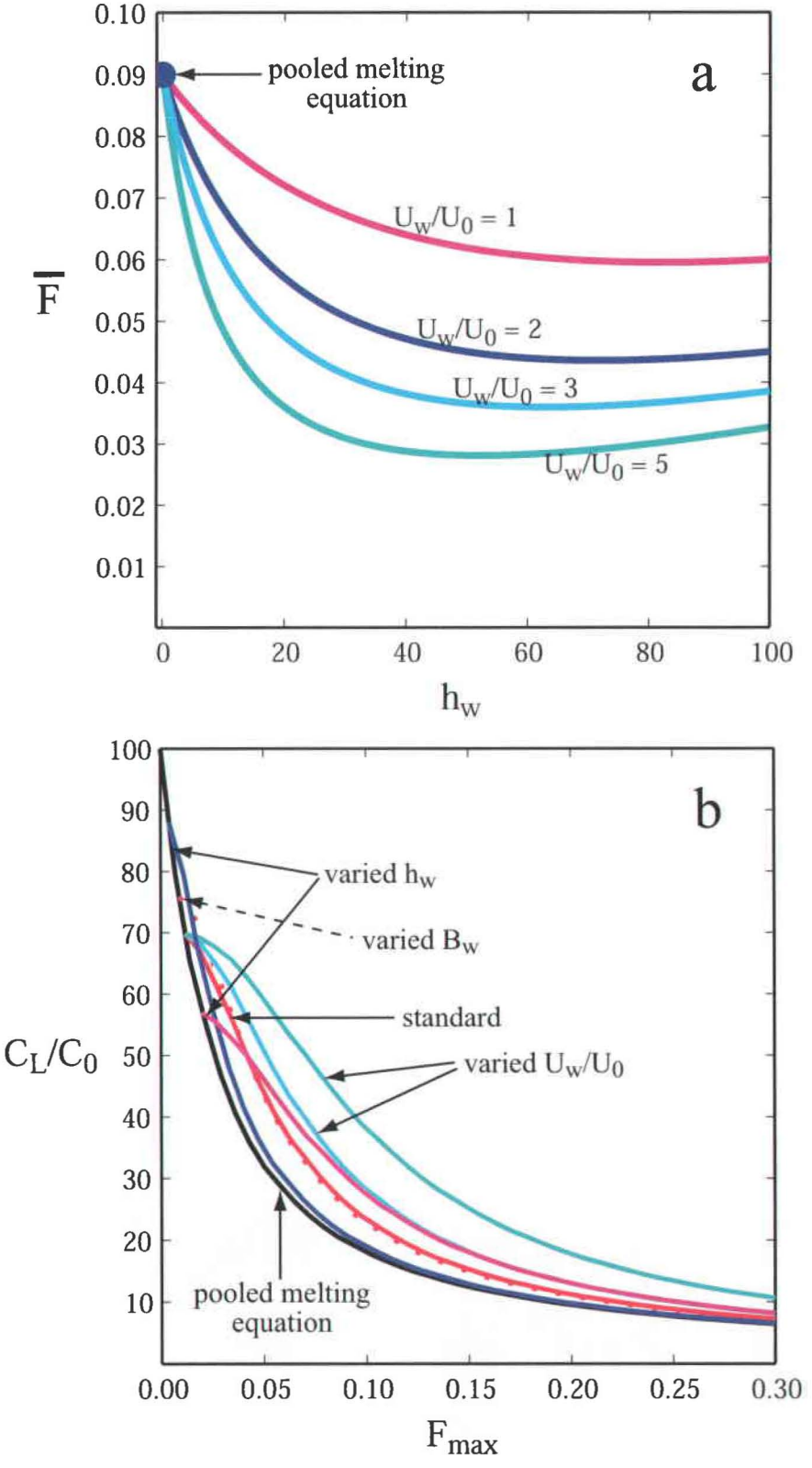
a
pooled melting equation
$U_w/U_0 = 1$
$U_w/U_0 = 2$
$U_w/U_0 = 3$
$U_w/U_0 = 5$
$\overline{F}$
h_w
b
varied h_w
varied B_w
standard
varied U_w/U_0
pooled melting equation
C_L/C_0
F_{max}

Figure 9

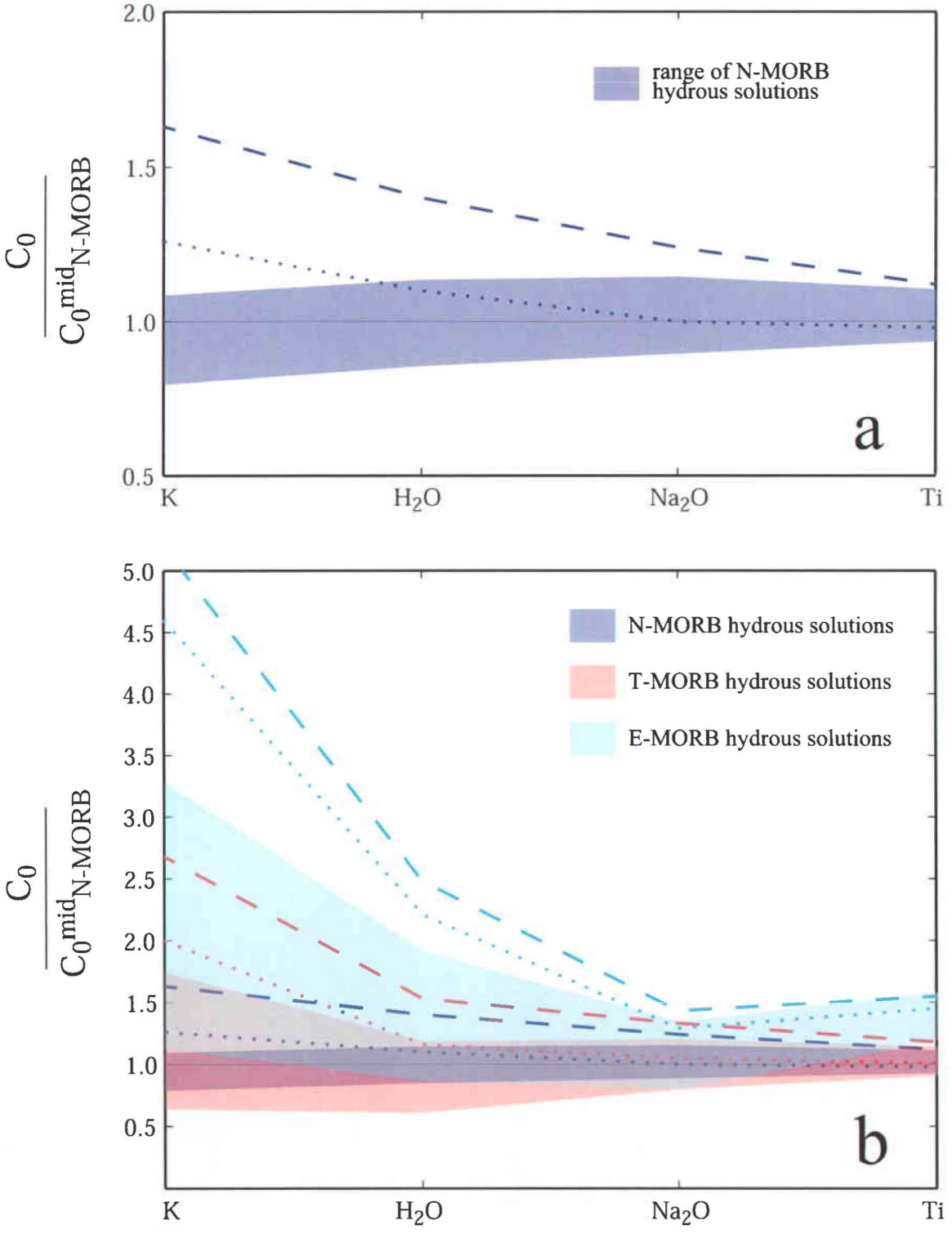
2.0
1.5
1.0
0.5
$C_0 / C_0^{mid}{}_{N\text{-}MORB}$
range of N-MORB hydrous solutions
a
K
H_2O
Na_2O
Ti
5.0
4.5
4.0
3.5
3.0
2.5
2.0
1.5
1.0
0.5
$C_0 / C_0^{mid}{}_{N\text{-}MORB}$
N-MORB hydrous solutions
T-MORB hydrous solutions
E-MORB hydrous solutions
b
K
H_2O
Na_2O
Ti

Figure 10

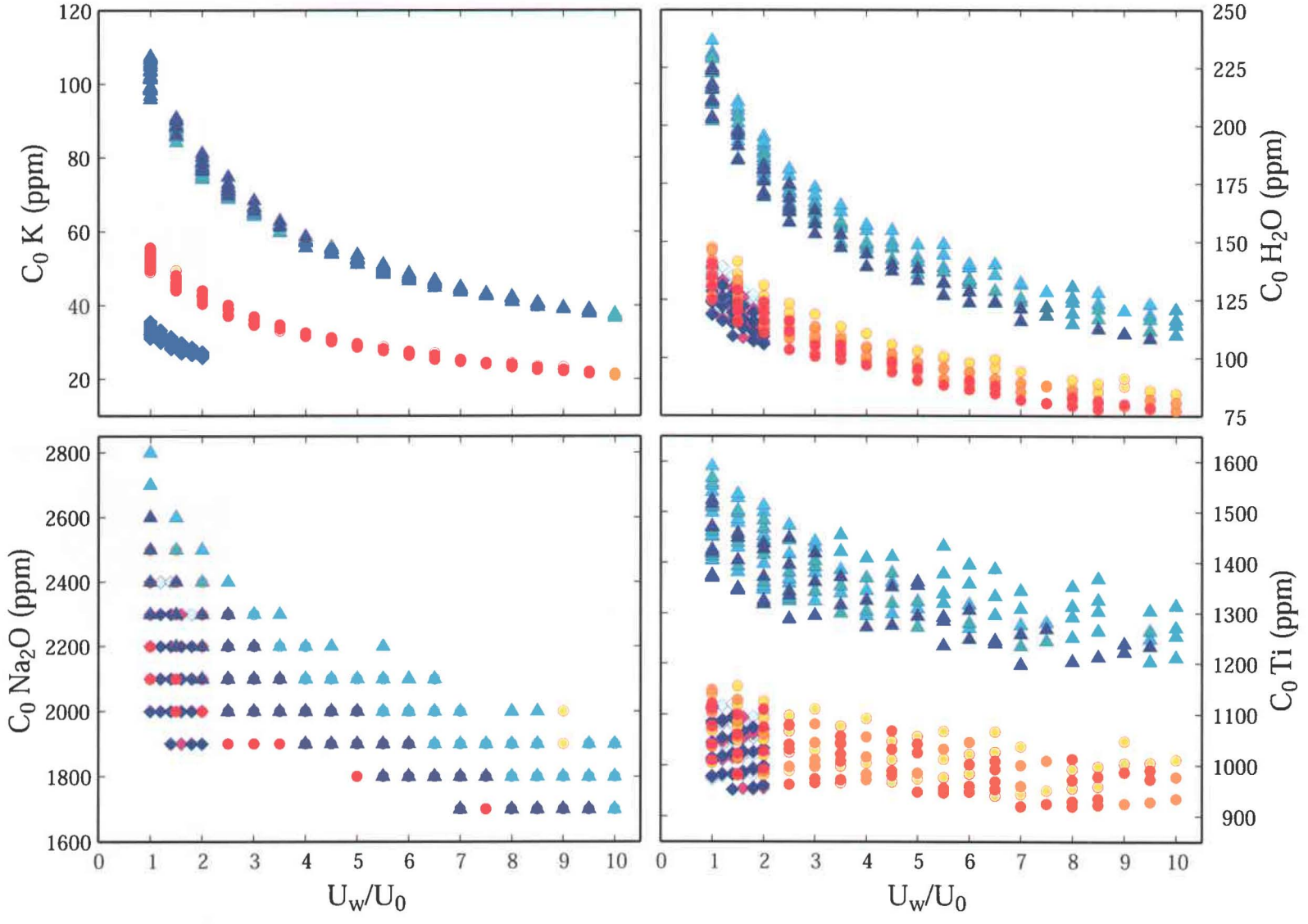

Figure 11

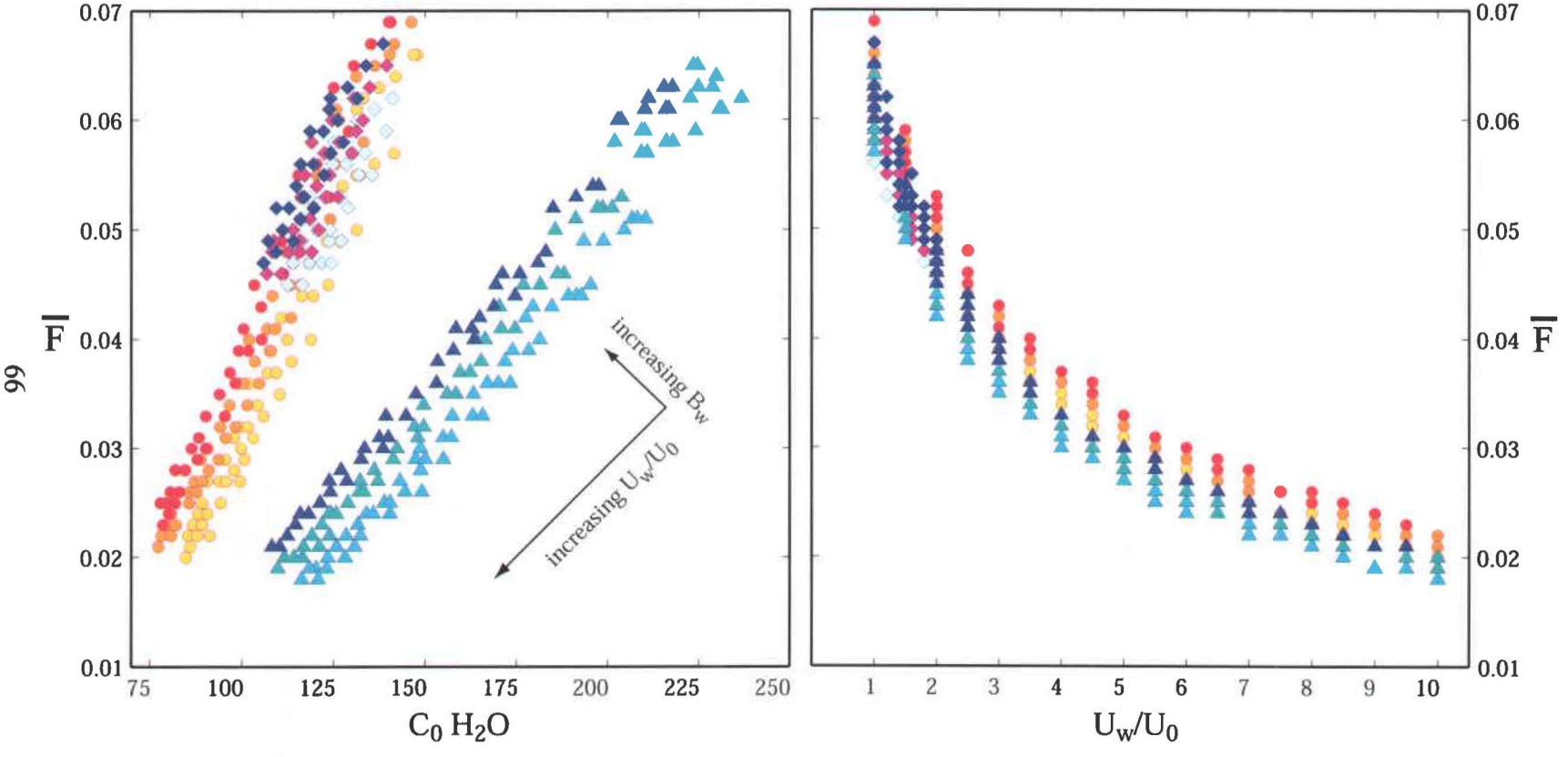
0.07
0.06
0.05
0.04
0.03
0.02
0.01
$\overline{F}$
75
100
125
150
175
200
225
250
$C_0\ H_2O$
increasing B_w
increasing U_w/U_0
1
2
3
4
5
6
7
8
9
10
U_w/U_0

Figure 12

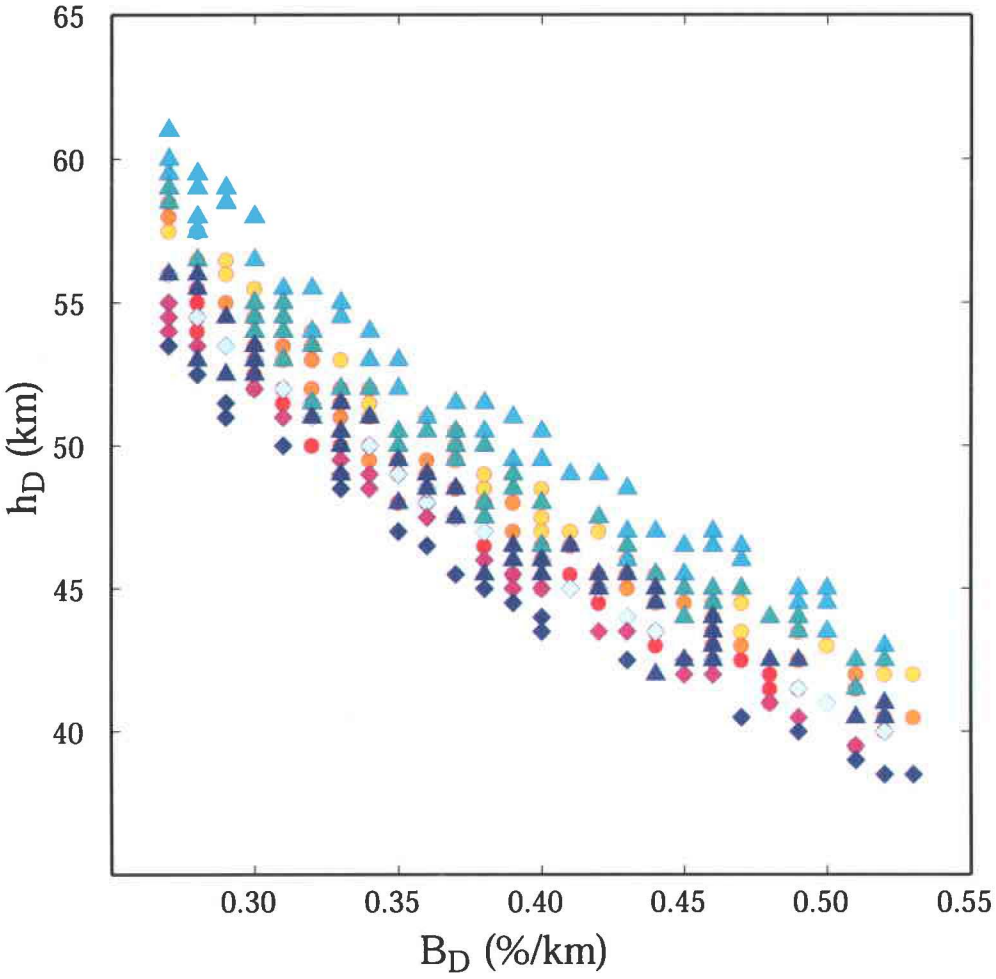

Figure 13

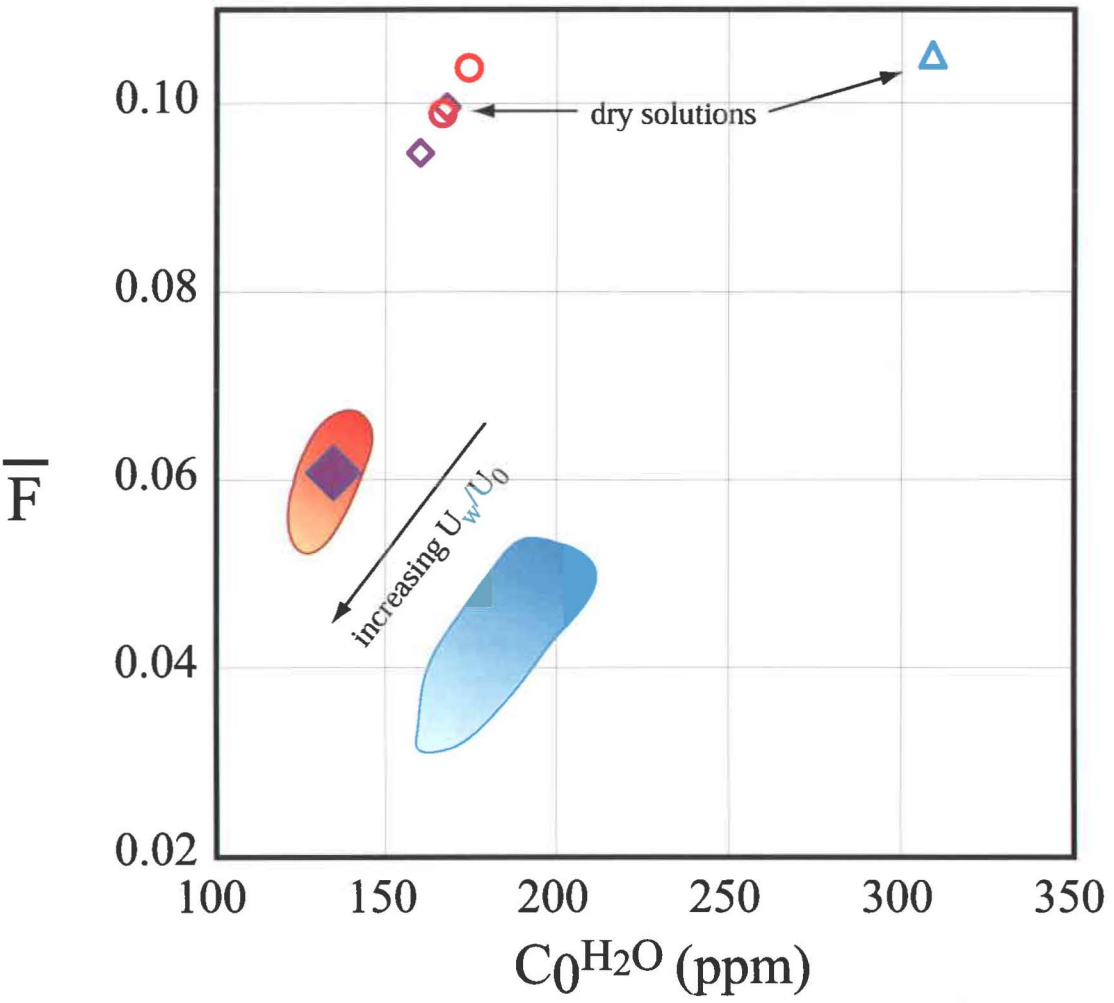
0.10
0.08
0.06
0.04
0.02
$\overline{F}$
dry solutions
increasing U_w/U_0
100
150
200
250
300
350
$C_0^{H_2O}$ (ppm)

Appendix

We collected S, F, and Cl data on one glass sample from each of 42 of the groups. These samples, which coincide with samples on which H_2O data were collected, were chosen based on major element geochemistry and along-axis locations. S, Cl, and F in glasses were analyzed using the University of Hawaii microprobe, following the procedures of Davis et al [2003]. Counting times were 200 seconds on peaks and 400 seconds on backgrounds, using an 80 nA beam current. Calibration standards were troilite (S), scapolite (Cl), and phlogopite (F). FeO was measured along with the volatiles to provide a correction for the interference of Fe on F [Todd, 1996]. Samples were calibrated multiple times during the run, using glass standards TR154_21D-3 and TR138_6D-1 for F and Cl, and Juan de Fuca glass standard VG-2 for S. No drift was observed. The major element content of each glass was used to apply the appropriate PAP-ZAF matrix correction. Reported values (Table 7) are the average of five spots.

Table 7. Halogen data in weight percent oxides

Group	Smpl #[a]	MORB-Type	F	S	Cl
2D	2D-1	N	0.0130	0.0964	0.0035
4D	4D-1	T3	0.0185	0.1187	0.0147
6D	6D-2*	T	0.0162	0.0798	0.0104
7D-a	7D-4	E	0.0320	0.1447	0.0599
9D-a	9D-1.1	T3	0.0278	0.1452	0.0405
10D	10D-1	E	0.0521	0.1849	0.1469
11D-a	11D-1	E	0.0838	0.1469	0.3362
12D	12D-5	E	0.0556	0.1852	0.1913
15D	15D-1	T3	0.0255	0.1245	0.0355
16D	16D-2	E2	0.0403	0.1334	0.0364
17D-a	17D-4	E2	0.0417	0.1104	0.0332
19D	19D-1	E	0.0540	0.1737	0.0875
20D-b	20D-1	E2	0.0322	0.1214	0.0261
23D	23D-2*	E	0.0362	0.1478	0.0279
25D-a	25D-1	E	0.0312	0.1295	0.0257
28D	28D-1	E	0.0290	0.1333	0.0276
29D	29D-1	T	0.0254	0.1491	0.0309
31D	31D-4*	T	0.0311	0.1611	0.0310
33D	33D-1	T	0.0250	0.1552	0.0227
38D	38D-2	T	0.0248	0.1556	0.0234
41D-b	41D-7	T	0.0170	0.1319	0.0162
41D-c	41D-1	T	0.0200	0.1419	0.0191
43D	43D-1	N	0.0115	0.1144	0.0070
45D	45D-2	T2	0.0215	0.1241	0.0151
46D	46D-1*	T	0.0157	0.1266	0.0134
48D-b	48D-4	T	0.0293	0.1545	0.0208
49D	49D-1	T	0.0300	0.1607	0.0224
50D	50D-1	T	0.0208	0.1247	0.0124
56D	56D-2	T	0.0210	0.1388	0.0121
58D	58D-2	T	0.0219	0.1492	0.0126
62D	62D-1	T3	0.0193	0.1293	0.0121
63D-a	63D-1	N	0.0181	0.1326	0.0087
63D-b	63D-2	T3	0.0216	0.1299	0.0115
67D	67D-1	T2	0.0199	0.1295	0.0152
69D	69D-1	T2	0.0227	0.1457	0.0261
70D	70D-1	T2	0.0227	0.1367	0.0181
71D-a	71D-1	N	0.0125	0.1036	0.0053
73D	73D-1	T	0.0158	0.1048	0.0050
75D	75D-1	N	0.0162	0.1366	0.0059
77D-a	77D-2	N	0.0182	0.1219	0.0046
78D-scor	78D-1	E2	0.0369	b	0.3984
79D	79D-1	N	0.0116	0.1141	0.0040
80D	80D-2	N	0.0174	0.1151	0.0040
84D	84D-4	N	0.0161	0.1191	0.0065
88D	88D-1	N	0.0109	0.1088	0.0054
92D	92D-1	N	0.0182	0.1213	0.0100

[a]Analyses were performed on sample numbers indicated; corresponding sample groups are noted. Asterisks indicate samples on which halogen data were collected, but H_2O analyses were *not* performed.
[b]S measurements on sample 78D are not reported because we were unable to reproduce analytical results.

References

Asimow, P.D., and C.H. Langmuir, The importance of water to oceanic melting regimes, *Nature, 421*, 815-820, 2003.

Asimow, P.D., M.M. Hirschmann, and E.M. Stolper, Calculation of peridotite partial melting from thermodynamic models of minerals and melts, IV. Adiabatic decompression and the composition and mean properties of mid-ocean ridge basalts, *Journal of Petrology, 42(5)*, 963-998, 2001.

Bell, D., G. Rossman, J. Maldener, D. Endisch, and F. Rauch, Hydroxide in olivine: A quantitative determination of the absolute amount and calibration of the IR spectrum, *Journal of Geophysical Research, 108*, 2105, 2003.

Bonatti, E., Not so hot "hot spots" in the oceanic mantle, *Science, 250*, 107-111, 1990.

Braun, M.G., G. Hirth, and E.M. Parmentier, The effects of deep damp melting on mantle flow and melt generation beneath mid-ocean ridges, *Earth and Planetary Science Letters, 176*, 339-356, 2000.

Canales, J.P., G. Ito, R.S. Detrick, and J. Sinton, Crustal thickness along the western Galápagos Spreading Center and the compensation of the Galápagos hotspot, *Earth and Planetary Science Letters*, 203, 311-327, 2002.

Canales, J.P., J. J. Danobeitia, R. S. Detrick, E.E.E. Hooft, R. Bartolomé, and D. Naar, Variations in axial morphology along the Galápagos Spreading Center and the influence of the Galápagos hotspot, *Journal of Geophysical Research, 102*, 27341-27354, 1997.

Christie, D. M., and J. M. Sinton, Major element constraints on melting, differentiation and mixing of magmas from the Galápagos 95.5°W propagating rift system, *Contributions to Mineralogy and Petrology, 94*, 274-288, 1986.

Christie, D. M., and J. M. Sinton, Evolution of abyssal lavas along propagating segments of the Galápagos Spreading Center, *Earth and Planetary Science Letters, 56*, 321-335, 1981.

Danyushevsky, L., S. Eggins, T. Falloon, and D. Christie, H_2O abundance in depleted to moderately enriched mid-ocean ridge magmas; part I: Incompatible behaviour, implications for mantle storage, and origin of regional variations, *Journal of Petrology, 41(8)*, 1329-1364, 2000.

Davis, M., M. Garcia, and P. Wallace, Volatiles in glasses from Mauna Loa Volcano, Hawaii: Implications for magma degassing and contamination, and growth of Hawaiian volcanoes, *Contributions to Mineralogy and Petrology, 144*, 570-591, 2003.

DeMets, C., R. G. Gordon, D. F. Argus, and S. Stein, Effect of recent revisions to the geomagnetic reversal time scale on estimates of current plate motions, *Geophysical Research Letters, 21*, 2191-2194, 1994.

Detrick, R. S., J.M. Sinton, G. Ito, J.P. Canales, M. Behn, T. Blacic, B. Cushman, J.E. Dixon, D.W. Graham, J.J. Mahoney, Correlated geophysical, geochemical and volcanological manifestations of plume-ridge interaction along the Galápagos Spreading Center, *Geochemistry, Geophysics, Geosystems, 3(10)*, doi:10. 1029/2002GC000350, 2002.

Dixon, J. E., and D. Clague, Volatiles in basaltic glasses from Loihi seamount, Hawaii: evidence for a relatively dry plume component, *Journal of Petrology, 42(3)*, 627-654, 2001.

Dixon, J.E., D. Clague, P. Wallace, and R. Poreda, Volatiles in alkalic basalts from the North Arch volcanic field, Hawaii: Extensive degassing of deep submarine-erupted alkalic series lavas, *Journal of Petrology, 38*, 911-939, 1997.

Dixon, J.E., D.A. Clague, and E.M. Stolper, Degassing history of water, sulfur, and carbon in submarine lavas from Kilauea Volcano, Hawaii, *Journal of Geology, 99*, 371-394, 1991.

Dixon, J.E., E.M. Stolper, and J.R. Delaney, Infrared spectroscopic measurements of CO_2 and H_2O glasses in the Juan de Fuca Ridge basaltic glasses, *Earth and Planetary Science Letters, 90*, 87-104, 1998.

Fisk, M. R., A. E. Bence, and J-G. Schilling, Major element chemistry of Galápagos rift zone magmas and their phenocrysts, *Earth and Planetary Science Letters, 61*, 171-189,1982.

Gaetani, G., and T. Grove, The influence of water on melting of mantle peridotite, *Contributions to Mineralogy and Petrology, 131*, 323-346, 1998.

Geist, D. J., An appraisal of melting processes and the Galápagos hotspot: major- and trace-element evidence, *Journal of Volcanology and Geothermal Research, 52*, 65-82, 1992.

Harpp, K, and D. Geist, Wolf-Darwin lineament and plume-ridge interaction in northern Galapagos, *Geochemistry, Geophysics, Geosystems, 3(11)*, doi: 10.1029/2002GC000370, 2002.

Hekenian, R., G. Thompson, and D. Bideau, Axial and off-axial heterogeneity of basaltic rocks from the East Pacific Rise at 12°35'N-12°51'N and 11°26'N-11°30'N, *Journal of Geophysical Research, 94*, 17437-17463, 1989.

Hey, R. N., J. M. Sinton, M. C. Kleinrock, R. N. Yonover, K. C. Macdonald, S. P. Miller, R. C. Searle, D. M. Christie, T. M. Atwater, N. H. Sleep, H. P. Johnson, and C. A. Neal, ALVIN Investigation of an active propagating rift system, Galápagos 95.5°W, *Marine Geophysical Research, 14*, 207-226, 1992.

Hirschmann, M. M., Mantle solidus: Experimental constraints and the effects of peridotite composition, *Geochemistry, Geophysics, Geosystems, 1*, 2000GC000070, 2000.

Hirschmann, M.M., P.D. Asimow, M.S. Ghiorso, and E.M. Stolper, Calculation of peridotite partial melting from thermodynamic models of minerals and melts. III. Controls on isobaric melt production and the effect of water on melt production, *Journal of Petrology, 40(5)*, 831-851, 1999.

Hirth, G., and D. Kohlstedt, Water in the oceanic upper mantle: implications for rheology, melt extraction and the evolution of the lithosphere, *Earth and Planetary Science Letters, 144*, 93-108, 1996.

Ihinger, P.D., R.L. Hervig, and P.F. McMillan, Applications of experimental results to C-O-H species in natural melts, *Mineralogical Society of America, Reviews in Mineralogy, 30*, 67-121, 1994.

Ito, G., Y. Shen, G. Hirth, and C. Wolfe, Mantle flow, melting, and dehydration of the Iceland mantle plume, *Earth and Planetary Science Letters, 165*, 81-96, 1999.

Johnson, K., H. Dick, and N. Shimizu, Melting in the oceanic upper mantle: An ion microprobe study of diopsides in abyssal peridotites, *Journal of Geophysical Research, 95*, 2661-2678, 1990.

Klein, E.M., T. Plank, and C. H. Langmuir, Constraints on models for mantle melting beneath ocean ridges, *RIDGE Events, 2*, 11-12, 1991.

Klein, E. and C. Langmuir, Global Correlations of Ocean Ridge Basalt Chemistry with Axial Depth and Crustal Thickness, *Journal of Geophysical Research, 92*, 8089-8115, 1987.

Kushiro, L, The system forsterite-diopside-silica with and without water at high pressure, *American Journal of Science, 267A*, 269-294, 1968.

Langmuir, C., E. Klein, and T. Plank, Petrological systematics of mid-ocean ridge basalts: constraints on melt generation beneath ocean ridges, mantle flow and melt generation at mid-ocean ridges, *AGU Monograph 71*, 184-280, 1992.

Maclennan, J., M. Jull, D. McKenzie, L. Slater, and K. Grönvold, The link between volcanism and deglaciation in Iceland, *Geochemistry, Geophysics, Geosystems, 3*(11), 1062, doi:10.1029/2001GC000282, 2002.

McKenzie, D. P., and M. J. Bickle, The volume and composition of melt generated by extension of the lithosphere, *Journal of Petrology, 29*, 625-679, 1988.

McKenzie, D., and R.K. O'Nions, Partial melt distributions from inversion of rare earth element concentrations, *Journal of Petrology, 32,* 1021-101, 1991.

Michael, P., Regionally distinctive sources of depleted MORB: Evidence from trace elements and H_2O, *Earth and Planetary Science Letters, 131*, 301-320, 1995.

Michael, P., The concentration, behavior and storage of H_2O in the suboceanic upper mantle: Implications for mantle metasomatism, *Geochemica et Cosmochimica Acta, 52*, 555-566, 1988.

Niu, Y., D. G. Waggoner, J. M. Sinton, and J. J. Mahoney, Mantle source heterogeneity and melting processes beneath seafloor spreading centers: The East Pacific Rise, 18°-19°S, *Journal of Geophysical Research, 101(B12)*, 27711-27733, 1996.

Phipps Morgan, J., and Y.J. Chen, Dependence of ridge-axis morphology on magma supply and spreading rate, *Nature, 364*, 706-708, 1993.

Plank, T., and C. Langmuir, Effects of the melting regime on the composition of the oceanic crust, *Journal of Geophysical Research, 97*, 19749-19770, 1992.

Schilling, J.G., M. Zajac, R. Evans, T. Johnston, W. White, J.D. Devine, and R. Kingsley, Petrologic and geochemical variations along the Mid-Atlantic Ridge from 29°N to 73°N, *American Journal of Science, 283*, 510-586, 1983.

Schilling, J.-G., R. H. Kingsley, and J. D. Devine, Galápagos hot spot-spreading center system I. Spatial petrological and geochemical variations (83°W-101°W), *Journal of Geophysical Research, 87*, 5593-5610, 1982.

Schilling, J.-G., M. B. Bergeron, and R. Evans, Halogens in the mantle beneath the North Atlantic, *Philosophical Transactions of the Royal Society of London, 297*, 147–178, 1980.

Shaw, D. M., Trace element fractionation during anatexis, *Geochemica et Cosmochimica Acta, 34*, 237–243, 1970.

Silver, L.A., P. D. Ihinger, and E. M. Stolper, The influence of bulk composition on the speciation of water in silicate glasses, *Contributions to Mineralogy and Petrology, 104*, 142-162, 1990.

Sinton, J. M., and R. S. Detrick, Mid-ocean ridge magma chambers, *Journal of Geophysical Research, 97*, 197-216, 1992.

Sinton, J.M., S. M. Smaglik, J. J. Mahoney, and K.C. MacDonald, Magmatic processes at superfast spreading midocean ridges: Glass compositional variations along the East Pacific Rise 13°-23°S, *Journal of Geophysical Research, 96*, 6133-6155, 1991.

Todd, C. S., Fluorine analysis by electron microprobe: Correction for iron interference. *Geological Society of America Abstracts, 28*, 212, 1996.

Verma, S. P., J-G. Schilling, and D. G. Waggoner, Neodymium isotopic evidence for Galápagos hotspot-spreading centre system evolution, *Nature, 306*, 654-657, 1983.

Verma, S. P., and J.-G. Schilling, Galápagos hot spot-spreading center system 2. $^{87}Sr/^{86}Sr$ and large ion lithophile element variations (85°W-101°W), *Journal of Geophysical Research, 87*, 10838-10856, 1982.

White, W. M., A. R. McBirney and R. A. Duncan, Petrology and geochemistry of the Galápagos Islands: portrait of a pathological mantle plume, *Journal of Geophysical Research, 98*, 19533-19563, 1993.

Yonover, R. N., 1989. Petrological effects of rift failure at the Galápagos Spreading Center near 95.5°W including analyses of glass inclusions by laser mass spectrometry and ion microprobe, Ph.D. Dissertation, University of Hawaii, Honolulu, 193 pp.